





# 3D synaptic organization of layer III of the human anterior cingulate and temporopolar cortex

Nicolás Cano-Astorga <sup>1,2,3</sup>, Sergio Plaza-Alonso <sup>1,2</sup>, Javier DeFelipe <sup>1,2,4</sup>, Lidia Alonso-Nanclares <sup>1,2,4,\*</sup>

<sup>1</sup>Laboratorio Cajal de Circuitos Corticales, Centro de Tecnología Biomédica, Universidad Politécnica de Madrid, Pozuelo de Alarcón, 28223 Madrid, Spain,

<sup>2</sup>Instituto Cajal, Consejo Superior de Investigaciones Científicas (CSIC), Avda. Doctor Arce 37, 28002 Madrid, Spain,

<sup>3</sup>PhD Program in Neuroscience, Autònoma de Madrid University - Cajal Institute, 28029 Madrid, Spain,

<sup>4</sup>Centro de Investigación Biomédica en Red sobre Enfermedades Neurodegenerativas (CIBERNED), ISCIII, Valderrebollo 5, 28031 Madrid, Spain

\*Corresponding author: Lidia Alonso-Nanclares, Laboratorio Cajal de Circuitos Corticales, Centro de Tecnología Biomédica, Universidad Politécnica de Madrid, Pozuelo de Alarcón, 28223 Madrid and Instituto Cajal, Consejo Superior de Investigaciones Científicas (CSIC), Avda. Doctor Arce 37, 28002 Madrid, Spain.

Email: [aidil@cajal.csic.es](mailto:aidil@cajal.csic.es)

The human anterior cingulate and temporopolar cortices have been proposed as highly connected nodes involved in high-order cognitive functions, but their synaptic organization is still basically unknown due to the difficulties involved in studying the human brain. Using Focused Ion Beam/Scanning Electron Microscopy (FIB/SEM) to study the synaptic organization of the human brain obtained with a short post-mortem delay allows excellent results to be obtained. We have used this technology to analyze layer III of the anterior cingulate cortex (Brodmann area 24) and the temporopolar cortex, including the temporal pole (Brodmann area 38 ventral and dorsal) and anterior middle temporal gyrus (Brodmann area 21). Our results, based on 6695 synaptic junctions fully reconstructed in 3D, revealed that Brodmann areas 24, 21 and ventral area 38 showed similar synaptic density and synaptic size, whereas dorsal area 38 displayed the highest synaptic density and the smallest synaptic size. However, the proportion of the different types of synapses (excitatory and inhibitory), the postsynaptic targets, and the shapes of excitatory and inhibitory synapses were similar, regardless of the region examined. These observations indicate that certain aspects of the synaptic organization are rather homogeneous, whereas others show specific variations across cortical regions.

**Key words:** autopsies; cerebral cortex; FIB-SEM; postsynaptic targets; ultrastructure.

## Introduction

Numerous studies focusing on the structural organization of the cerebral cortex have been obtained from experimental animals and, in general, it is assumed that these data can be extrapolated to the human cerebral cortex. However, certain fundamental structural and behavioral characteristics are unique to humans and it is therefore imperative to acquire data directly from human brains (e.g. DeFelipe 2015; Mansvelder et al. 2019). Autopsy samples may be the sole source of strictly normal tissue, but the ultrastructure of the post-mortem brain tissue (often obtained 5 or more hours after death) is generally not well preserved, making the tissue unsuitable for detailed quantitative analysis. Therefore, synaptic circuitry data for the normal human brain is virtually non-existent.

However, excellent results have recently been shown in the analysis of human autopsy brain microanatomy after applying a variety of techniques to study brain tissue if it is collected with a post-mortem delay of less than 4 h. These techniques include intracellular injections to visualize the detailed morphology of neurons (e.g. Benavides-Piccione et al. 2021) and 3D electron microscopy methods using Focused Ion Beam/Scanning Electron Microscopy (FIB/SEM; e.g. Montero-Crespo et al. 2020; Cano-Astorga et al. 2021).

In the present study, we have used FIB/SEM to analyze non-pathological brain tissue samples obtained from autopsy cases

with a post-mortem delay of less than 4 h. The goal was to study the normal synaptic organization of the neuropil, where the vast majority of synapses are found (DeFelipe et al. 1999). This technology was chosen because the images obtained are similar to those obtained with transmission electron microscopy, but with the advantage that FIB/SEM permits serial reconstructions of large volumes of tissue to be generated rapidly and automatically (Merchán-Pérez et al. 2009), facilitating detailed 3D reconstructions of synaptic junctions and the extraction of synaptic data, even from the human cerebral cortex (Blázquez-Llorca et al. 2013; Domínguez-Álvaro et al. 2018, 2019, 2021a, 2021b; Montero-Crespo et al. 2020, 2021; Cano-Astorga et al. 2021).

We focused on Brodmann area (BA) 24, 38 (ventral and dorsal) and 21 (see Zilles and Amunts 2010), as representative areas of the anterior cingulate (BA24) and temporopolar cortices, including the temporal pole (BA38) and anterior middle temporal gyrus (BA21) (see Mesulam 2022). It has been proposed that these cortical regions are critically involved in the emergence of a variety of high-order cognitive functions such as memory (Damasio et al. 1990; Wang et al. 2021; Fuster 2022; Mesulam 2022); socio-emotional processing and language (Damasio et al. 1996; Kondo et al. 2003; Olson et al. 2013; Xu et al. 2016; Joyce et al. 2022); attention and learning (Morecraft et al. 1993; Keogh et al. 2022); and object/face recognition (Morán et al. 1987; Nakamura and Kubota 1996; Pascual et al. 2015; Levakov et al. 2021).

Received: April 11, 2023. Revised: June 8, 2023. Accepted: June 9, 2023

© The Author(s) 2023. Published by Oxford University Press. All rights reserved. For permissions, please e-mail: [journals.permissions@oup.com](mailto:journals.permissions@oup.com)

This is an Open Access article distributed under the terms of the Creative Commons Attribution Non-Commercial License (<http://creativecommons.org/licenses/by-nc/4.0/>), which permits non-commercial re-use, distribution, and reproduction in any medium, provided the original work is properly cited. For commercial re-use, please contact [journals.permissions@oup.com](mailto:journals.permissions@oup.com)

Finally, as 3D electron microscopy is very time-consuming, we chose layer III because it plays a key role in the cortico-cortical circuits (Thomson and Lamy 2007; D'Souza and Burkhalter 2017), and most of the physiological and morphological studies in the human neurons have been performed in layers II and III (e.g. see Eyal et al. 2018; Gidon et al. 2020; Benavides-Piccione et al. 2021, and references therein). Therefore, the detailed ultrastructural analysis performed in the present study would contribute to a better understanding of this layer of the human cerebral cortex.

## Material and methods

### Tissue preparation

Human brain tissue was obtained from three autopsies (with short postmortem delays of less than 4 h) obtained from two men (53 and 66 years old) and one woman (53 years old) with no recorded neurological or psychiatric alterations. The procedure was approved by the Institutional Ethical Committee. This human brain tissue has been used in previous studies (Domínguez-Álvarez et al. 2018, 2019, 2021a; Montero-Crespo et al. 2020; Cano-Astorga et al. 2021).

Regarding the particular location of the sampled cortical areas, and in order to make a comprehensive correlation with the relevant literature, our samples from BA24 correspond to the “p24b” field defined in Palomero-Gallagher et al. (2008). BA38 has been distinguished at cytoarchitectonic (Ding et al. 2009; Blaizot et al. 2010; Insausti 2013), connectivity (Kondo et al. 2003) and functional (Pascual et al. 2015) levels into many subdivisions. Thus, we have differentiated ventral BA38 (vBA38), which corresponds to the “TG” area defined in Ding et al. (2009), and dorsal BA38 (dBA38), which corresponds to the “TA” area defined in Ding et al. (2009). BA21 corresponds to the middle temporal gyrus (T2).

After extraction, the brain tissue was fixed in cold 4% paraformaldehyde (Sigma-Aldrich, St Louis, MO, USA) in 0.1 M sodium phosphate buffer (PB; Panreac, 131965, Spain), pH 7.4 for 24–48 h. After fixation, blocks of tissue of approximately 1 cm × 1 cm × 1 cm were washed in PB and sectioned coronally in a vibratome (150 μm thickness; Vibratome Sectioning System, VT1200S Vibratome, Leica Biosystems, Germany). Sections containing BA24, vBA38, dBA38, and BA21 were selected and processed for Nissl staining to determine cytoarchitecture (Fig. 1).

### Volume fraction estimation of cortical elements

Semithin sections (1–1.5 μm thick) from all cases stained with toluidine blue (see below) were used to estimate the respective volume fraction (Vv) occupied by (i) neuropil, (ii) cell bodies (from neurons, glia, and undetermined somata), and (iii) blood vessels. This estimation was performed applying the Cavalieri principle to 12 semithin sections per case (Gundersen et al. 1988) by point counting (Q-) using the integrated Stereo Investigator stereological package (Version 8.0, MicroBrightField Inc., VT, USA) attached to an Olympus light microscope (Olympus, Bellerup, Denmark) at 40× magnification. A grid, whose points covered an area of 2,500 μm<sup>2</sup>, was randomly placed at six sites over the traced layer III on each semithin section to determine the Vv occupied by the different elements: neuropil, cell bodies, and blood vessels (Fig. 2). Vv (e.g. in the case of the neuropil) was estimated with the following formula:  $Vv\text{-neuropil} = Q\text{-neuropil} \times 100 / (Q\text{-neuropil} + Q\text{-neurons} + Q\text{-glia} + Q\text{-undetermined cells} + Q\text{-blood vessels})$ .

### Electron microscopy processing

Sections containing BA24, vBA38, dBA38, and BA21 were selected, washed in 0.1 M PB and postfixated for 24 h in a solution

containing 2% paraformaldehyde, 2.5% glutaraldehyde (TAAB, G002, UK), and 0.003% CaCl<sub>2</sub> (Sigma, C-2661-500G, Germany) in sodium cacodylate (Sigma, C0250-500G, Germany) buffer (0.1 M). The sections were treated with 1% OsO<sub>4</sub> (Sigma, O5500, Germany), 0.1% potassium ferrocyanide (Probus, 23,345, Spain), and 0.003% CaCl<sub>2</sub> in sodium cacodylate buffer (0.1 M) for 1 h at room temperature. They were then stained with 1% uranyl acetate (EMS, 8473, USA), dehydrated, and flat-embedded in Araldite (TAAB, E021, UK) for 48 h at 60°C (DeFelipe and Fairén 1993). The embedded sections were then glued onto a blank Araldite block. Semithin sections (1–2 μm thick) were obtained from the surface of the block and stained with 1% toluidine blue (Merck, 115930, Germany) in 1% sodium borate (Panreac, 141644, Spain). The last semithin section (which corresponds to the section immediately adjacent to the block surface) was examined under light microscope and photographed to accurately locate the neuropil regions to be examined (Fig. 1).

### Three-dimensional Electron microscopy

The 3D study of the samples was carried out using a dual beam microscope (Crossbeam® 40 electron microscope, Carl Zeiss NTS GmbH, Oberkochen, Germany). This instrument combines a high-resolution field-emission SEM column with a focused gallium ion beam (FIB), which permits removal of thin layers of material from the sample surface on a nanometer scale. As soon as one layer of material (20 nm thick) is removed by the FIB, the exposed surface of the sample is imaged by the SEM using the backscattered electron detector. The sequential automated use of FIB milling and SEM imaging allowed us to obtain long series of photographs of a 3D sample of selected regions (Merchán-Pérez et al. 2009). Image resolution in the xy plane was 5 nm/pixel. Resolution in the z-axis (section thickness) was 20 nm, and image size was 2048 × 1536 pixels. These parameters were chosen in order to obtain a large enough field of view where synaptic junctions could be clearly identified, within a reasonable time frame (approximately 12 h per stack of images). The number of sections per stack ranged from 240–330 in BA24, 254–314 in vBA38, 261–305 in dBA38, and 260–317 in BA21, which corresponds to a volume per stack ranging from 623–856 μm<sup>3</sup> (mean: 709 μm<sup>3</sup>) in BA24, 654–815 μm<sup>3</sup> (mean: 726 μm<sup>3</sup>) in vBA38, 678–792 μm<sup>3</sup> (mean: 716 μm<sup>3</sup>) in dBA38, and 675–822 μm<sup>3</sup> (mean: 744 μm<sup>3</sup>) in BA21. We acquired nine stacks of images (layer III; approximately 600–1,100 μm from the pial surface) in BA24 (three stacks per case, in three cases; total volume studied: 4,289 μm<sup>3</sup>); nine stacks of images (approximately 700–800 μm from the pial surface) in vBA38 (three stacks per case, in three cases; total volume studied: 4,399 μm<sup>3</sup>); nine stacks of images (approximately 600–900 μm from the pial surface) in dBA38 (three stacks from three cases; total volume studied: 4,336 μm<sup>3</sup>); and seven stacks of images (approximately 600 μm from the pial surface) in BA21 (two stacks of images per case in cases AB2 and AB3 taken from Cano-Astorga et al. (2021), and three stacks of images in case AB7; total volume studied: 3,896 μm<sup>3</sup>). Examples of the serial images obtained in each cortical region are illustrated in Fig. 3.

All measurements were corrected for tissue shrinkage, which occurs during the processing of sections (Merchán-Pérez et al. 2009). To estimate the shrinkage in our samples, we photographed and measured the area of the vibratome sections with ImageJ (ImageJ 1.51; NIH, USA), both before and after processing for electron microscopy. The section area values after processing were divided by the values before processing to obtain the volume, area, and linear shrinkage factors (Oorschot et al. 1991)—yielding correction factors of 0.90, 0.93, and 0.97, respectively.



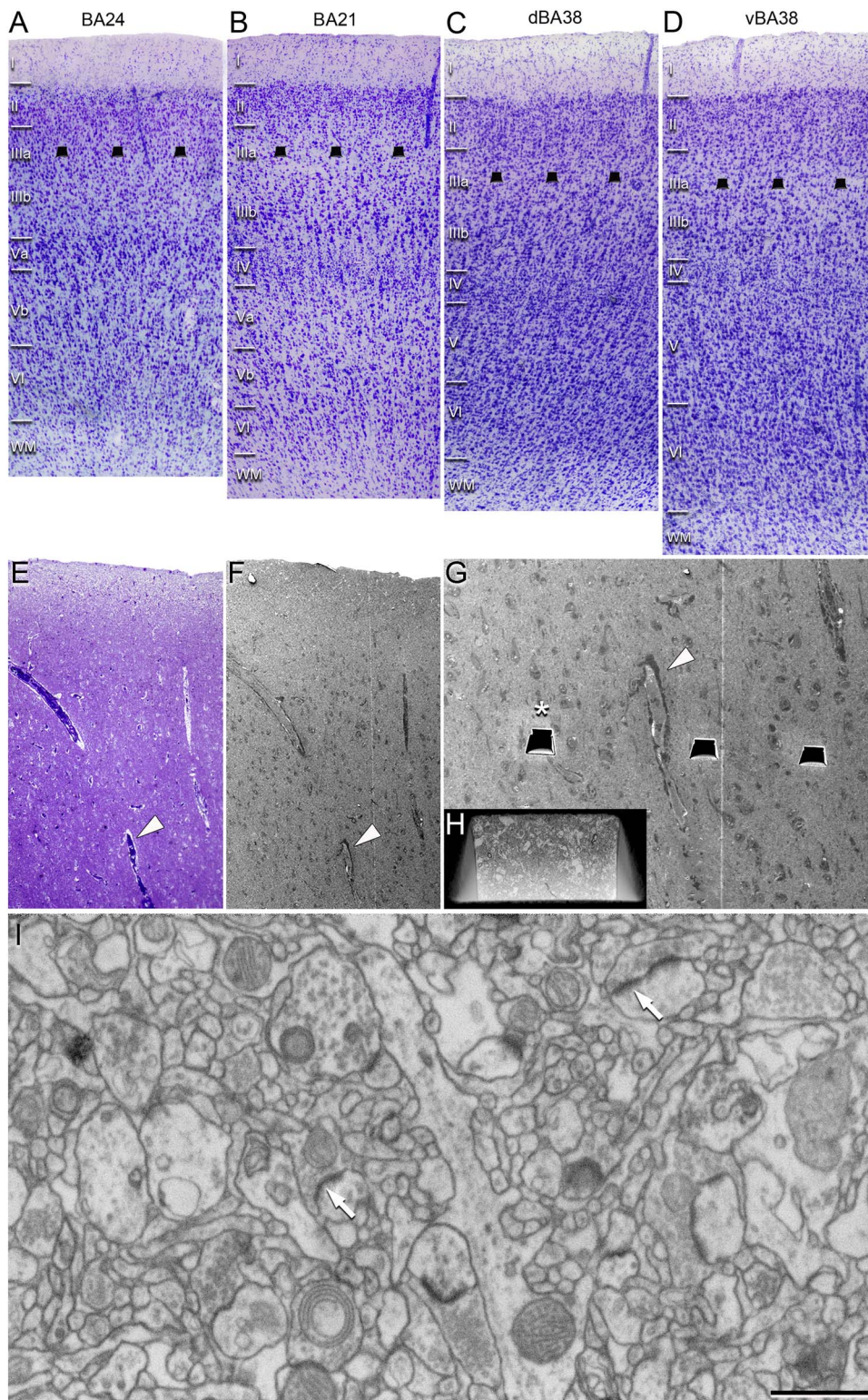


**Fig. 1.** Cortical and FIB/SEM sampling regions. (A–D) Nissl-stained sections to illustrate the cytoarchitectonic differences between regions from an autopsy case. Cortical layer delimitation based on Palomero-Gallagher et al. (2008) for (A), Alonso-Nanclares et al. (2008) in (B), and Ding et al. (2009) for (C) and (D). Illustration of the analyzed FIB/SEM sampling regions (superimposed as dark trapezoids in A–D). (E–G) Correlative light/electron microscopy analyses of layer III neuropil. (E) 1- $\mu\text{m}$ -thick semithin section stained with toluidine blue, which is adjacent to the block for FIB/SEM imaging (F). (F) SEM image illustrating the block surface. (G) Higher magnification of (F), showing the trenches made in the neuropil to acquire the FIB/SEM stacks of images. White arrowheads in (E), (F), and (G) point to the same blood vessel, allowing the exact location of the region of interest to be identified. (H) SEM image at higher magnification showing the front of a trench (white asterisk in G) made to acquire an FIB/SEM stack of images. (I) FIB/SEM image from a stack of images. Two synapses are indicated (arrows). Scale bar (in D) indicates 320  $\mu\text{m}$  for (A)–(D); 200  $\mu\text{m}$  for (E)–(F); 80  $\mu\text{m}$  in (G); 15  $\mu\text{m}$  in (H); 1.20  $\mu\text{m}$  in (I). BA: Brodmann area; d: dorsal; v: ventral.



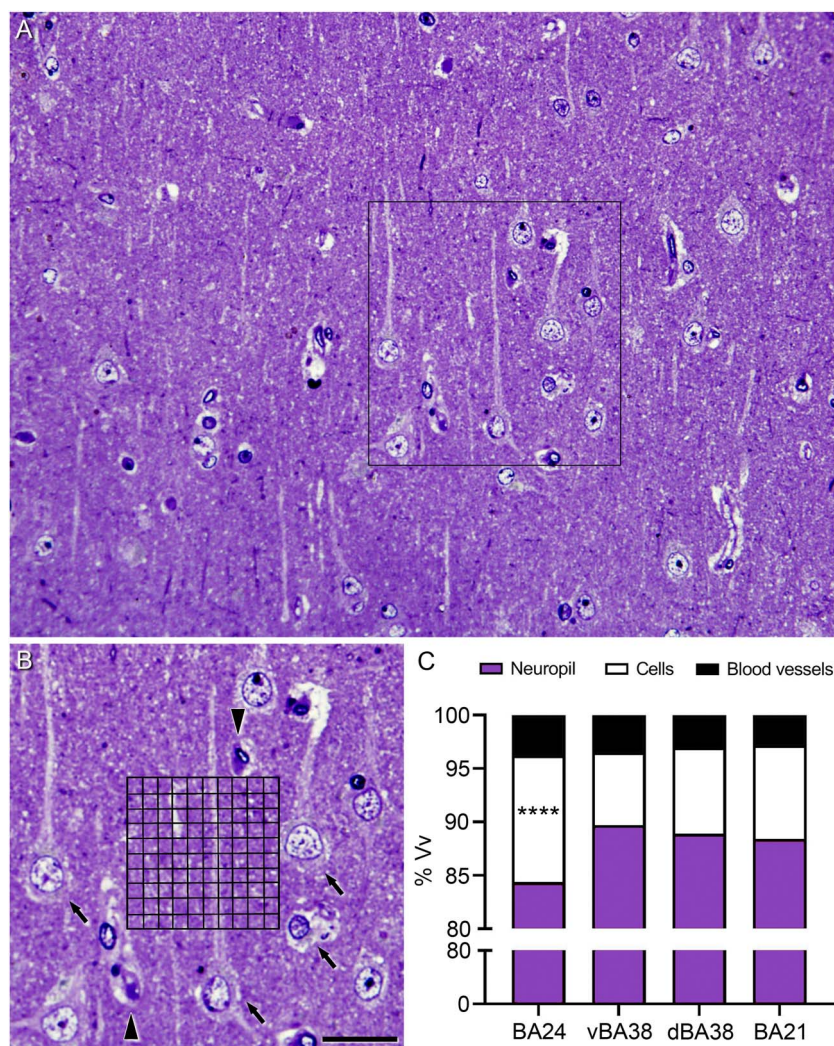


**Fig. 2.** Stereological estimation of the volume fraction occupied by different cortical elements in BA24, vBA38, dBA38, and BA21. (A) Low-power micrograph of a toluidine blue-stained 1.5- $\mu$ m-thick semithin section of vBA38. (B) High-power magnification of the boxed area in (A) showing a 50  $\mu$ m  $\times$  50  $\mu$ m grid superimposed on the original micrograph, where points hitting the different cortical elements were counted. Some blood vessels (arrowheads) and cell bodies (arrows) are indicated. (C) Plot of the volume fraction occupied by each analyzed cortical element. BA24 shows a higher volume fraction occupied by cells than the other cortical regions ( $\chi^2$ ,  $P < 0.001$ ). Scale bar (in B) indicates 40  $\mu$ m in (A), and 25  $\mu$ m in (B). BA: Brodmann area; d: dorsal; v: ventral.

Nevertheless, in order to compare with previous studies—in which either no correction factors had been included or such factors were estimated using other methods—in the present study, we provided both sets of data. Additionally, a correction in the volume of the stack of images—to account for the presence of fixation artifact (i.e. swollen neuronal or glial processes)—was applied after quantification with Cavalieri principle (Gundersen et al. 1988; see Montero-Crespo et al. 2020). Every FIB/SEM stack was examined, and the volume artifact was found to range from 0.0 to 16.1% of the volume stacks.

### Three-dimensional analysis of synapses

Stacks of images obtained by the FIB/SEM were analyzed using EspINA software (EspINA Interactive Neuron Analyzer, 2.9.12; <https://cajalbbp.es/espina/>; Morales et al. 2011; Fig. 4). As previously discussed (Merchán-Pérez et al. 2009), there is a consensus for classifying cortical synapses into asymmetric synapses (AS; or type I) and symmetric synapses (SS; or type II). The main characteristic distinguishing these synapses is their prominent or thin postsynaptic density (PSD), respectively (Supplementary Fig. 1).

Also, these two types of synapses correlate with different functions: AS are mostly glutamatergic and excitatory, while SS are mostly GABAergic and inhibitory (DeFelipe and Fariñas 1992; DeFelipe et al. 1999). Nevertheless, in single sections, the synaptic cleft and the pre- and postsynaptic densities are often blurred if the plane of the section does not pass at right angles to the synaptic junction. As the software EspINA allows navigation through the stack of images, it was possible to unambiguously identify every synapse as AS or SS based on the thickness of the PSD (Merchán-Pérez et al. 2009).

Synapses with prominent PSDs are classified as AS, while those with thin PSDs are classified as SS (Gray 1959; Peters et al. 1991; Supplementary Fig. 1). In addition, geometrical features—such as size and shape—and spatial distribution features (centroids) of each reconstructed synaptic junction were also calculated by EspINA. The EspINA software tool facilitates the 3D reconstruction of the pre- and post-synaptic membranes of the synaptic junction, which we will refer to as “3D reconstructed synaptic junction”. This software also extracts the Synaptic Apposition Area (SAS) and provides its measurements. Given that the pre- and postsynaptic densities are located face to face, their surface areas

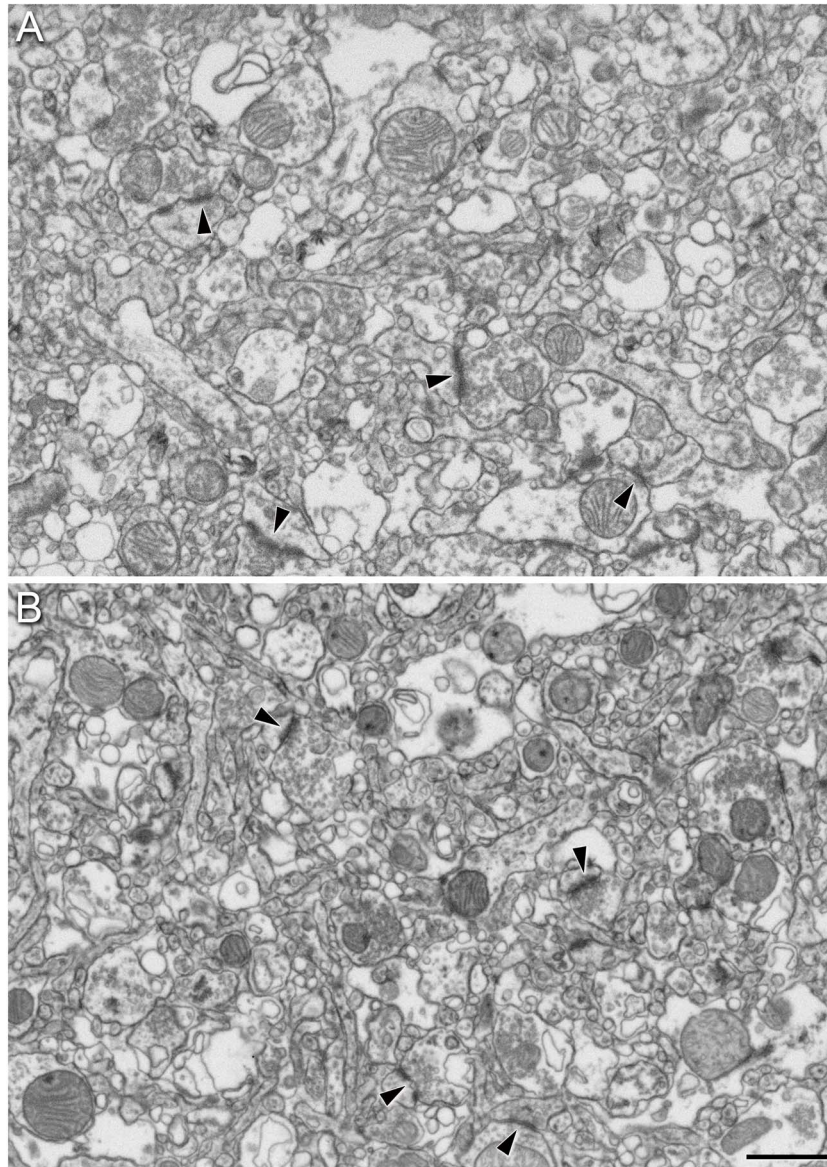


**Fig. 3.** Images obtained by FIB/SEM showing neuropil of vBA38 (A), and BA21 (B) from an autopsy case (AB3). Some examples of synapses are indicated in all regions (arrowheads). Scale bar (in B) indicates 1  $\mu$ m in (A–B). BA: Brodmann area; d: dorsal; v: ventral.

are comparable (for details, see [Morales et al. 2013](#); [Fig. 5A, B](#)). As the SAS comprises both the active zone and the PSD, it is a functionally relevant measure of the size of a synaptic junction ([Morales et al. 2013](#)). EspINA was also used to visualize each of the reconstructed synaptic junction in 3D and to detect the possible presence of perforations or deep indentations in their perimeters. Regarding the shape of the PSD, the synapses could be classified into four main categories, according to the categories proposed by [Santuy et al. \(2018a\)](#): macular (disk-shaped PSD), perforated (with one or more holes in the PSD), horseshoe-shaped (with an indentation), and fragmented (disk-shaped PSDs with no connection between them) ([Fig. 5C](#)). To identify the postsynaptic targets of the synapses, we navigated through the image stack using EspINA to determine whether the postsynaptic element was a dendritic spine (spine, for simplicity) or a dendritic shaft. As previously described in [Domínguez-Álvaro et al. \(2021a, 2021b\)](#), unambiguous identification of spines requires the spine to be visually traced to the parent dendrite (see [Cano-Astorga et al. 2021](#)), in which case we refer to them as complete spines. When

synapses were established on a spine head-shaped postsynaptic element whose neck could not be followed to the parent dendrite, we identified these elements as incomplete spines. These incomplete spines were identified on the basis of their size and shape, the lack of mitochondria, and the presence of a spine apparatus—or because they were filled with “fluffy material” (a term coined by [Peters et al. \(1991\)](#) to describe the fine and indistinct filaments present in the spines; see also [del Río and DeFelipe 1995](#)). For simplicity, we will refer to both the complete and incomplete spines as spines, unless otherwise specified. We also recorded the presence of single or multiple synapses on a single spine. Furthermore, we determined whether the target dendrite had spines or not.

### Quantification of the synaptic density

EspINA provided the 3D reconstruction of every synapse and allowed the application of an unbiased 3D counting frame (CF)—a regular prism enclosed by three acceptance planes and three exclusion planes marking its boundaries. All objects within



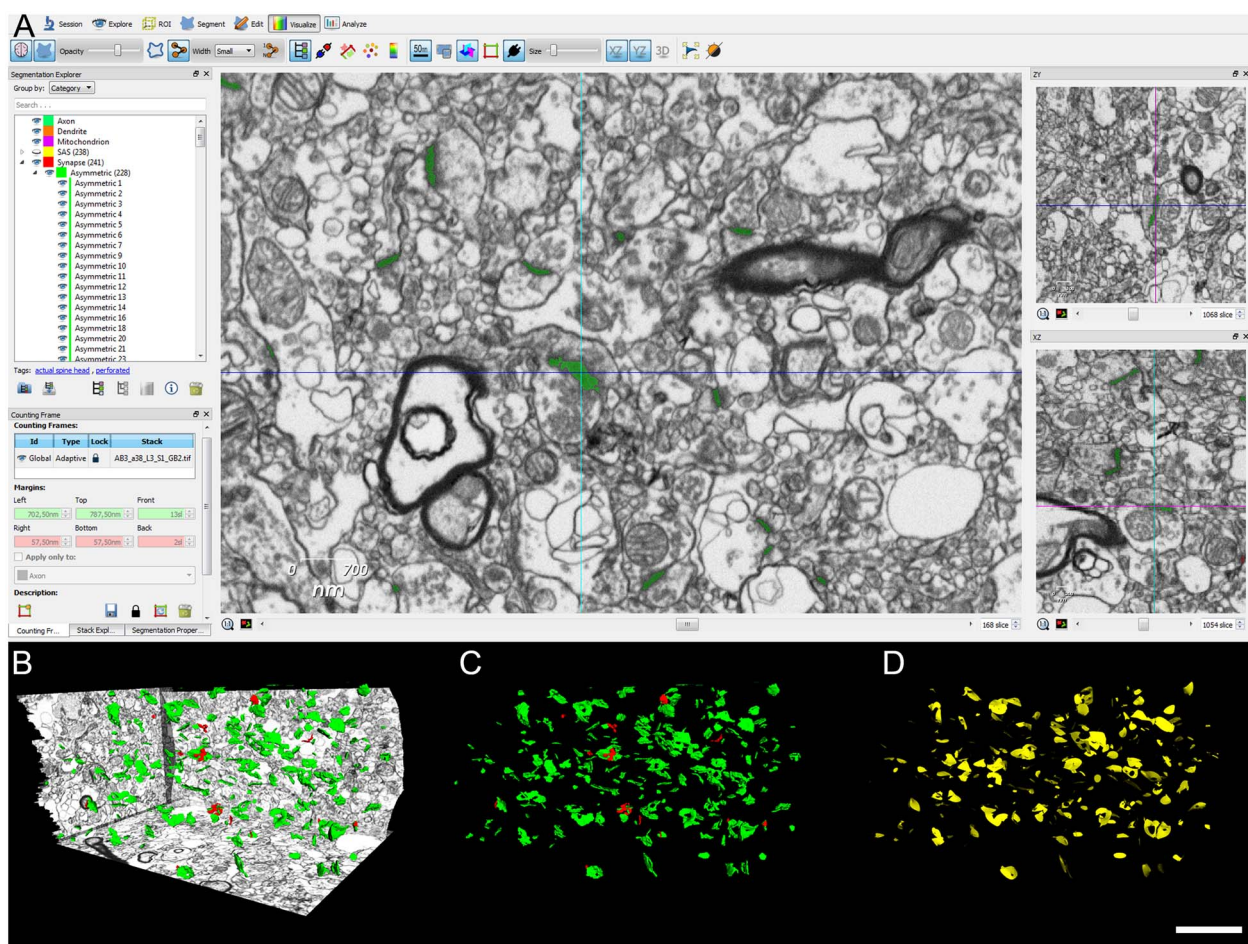


**Fig. 4.** Three-dimensional analysis of synapses. Identification and annotation of synapses. (A–D) Screenshots of the EspINA software user interface. (A) In the main window, the sections are viewed through the xy plane (as obtained by FIB/SEM microscopy). The other two orthogonal planes, yz and xz, are also shown in adjacent windows (on the right). (B) The 3D window shows the three orthogonal planes and the 3D reconstruction of asymmetric (green) and symmetric (red) synaptic junctions. (C) 3D reconstructed synaptic junction displayed by colors. (D) Computed synaptic apposition surface for each reconstructed synaptic junction (yellow). Scale bar (in D) indicates 2.6  $\mu\text{m}$ , for (B)–(D).

the CF are counted, as are those intersecting any of the acceptance planes, whereas objects that are outside the CF, or intersecting any of the exclusion planes, are not counted. Thus, the number of synapses per unit volume was calculated directly by dividing the total number of synapses counted by the volume of the CF (Merchán-Pérez et al. 2009). This method was used in all 37 stacks of images (three stacks of images per case, in three cases in BA24, vBA38, dBA38; two stacks of images per case in cases AB2 and AB3, taken from Cano-Astorga et al. (2021), and three stacks of images in case AB7 in BA21).

### Spatial distribution analysis of synapses

To analyze the spatial distribution of synapses, spatial point pattern analysis was performed as described elsewhere (Antón-Sánchez et al. 2014; Merchán-Pérez et al. 2014). Briefly, we compared the actual position of centroids of synaptic junctions with the CSR model—a random spatial distribution model that defines a situation where a point is equally likely to occur at any location within a given volume. For each of the 37 FIB/SEM stacks of images, we calculated three functions commonly used for spatial point pattern analysis: G, F, and K functions (Supplementary Fig. 2). As described in Merchán-Pérez et al. (2014) (see also Antón-Sánchez et al. 2014), the G function, also called the nearest-neighbor distance cumulative distribution function or the

event-to-event distribution, is—for a distance  $d$ —the probability that a typical point separates from its nearest neighbor by a distance of  $d$  at the most. The F function, also known as the empty space function or the point-to-event distribution, is—for a distance  $d$ —the probability that the distance of each point (in a regularly spaced grid of  $L$  points superimposed over the sample) to its nearest synaptic junction centroid is  $d$  at the most. The K function, also called the reduced second moment function or Ripley's function, is—for a distance  $d$ —the expected number of points within a distance  $d$  of a typical point of the process divided by the intensity  $\lambda$ . An estimation of the K function is given by the mean number of points within a sphere of increasing radius  $d$  centered on each sample point, divided by an estimation of the expected number of points per unit volume. This study was carried out using the Spatstat package and R Project program (Baddeley et al. 2015).

### Statistical analysis

One-way analyses of variance (ANOVA) with Holm-Sidak's post-hoc correction was performed to compare the synaptic density between regions. To perform statistical comparisons of AS:SS proportions regarding their synaptic shape and their postsynaptic targets, chi-square ( $\chi^2$ ) test was used for contingency tables. The same method was used to obtain comparisons between regions

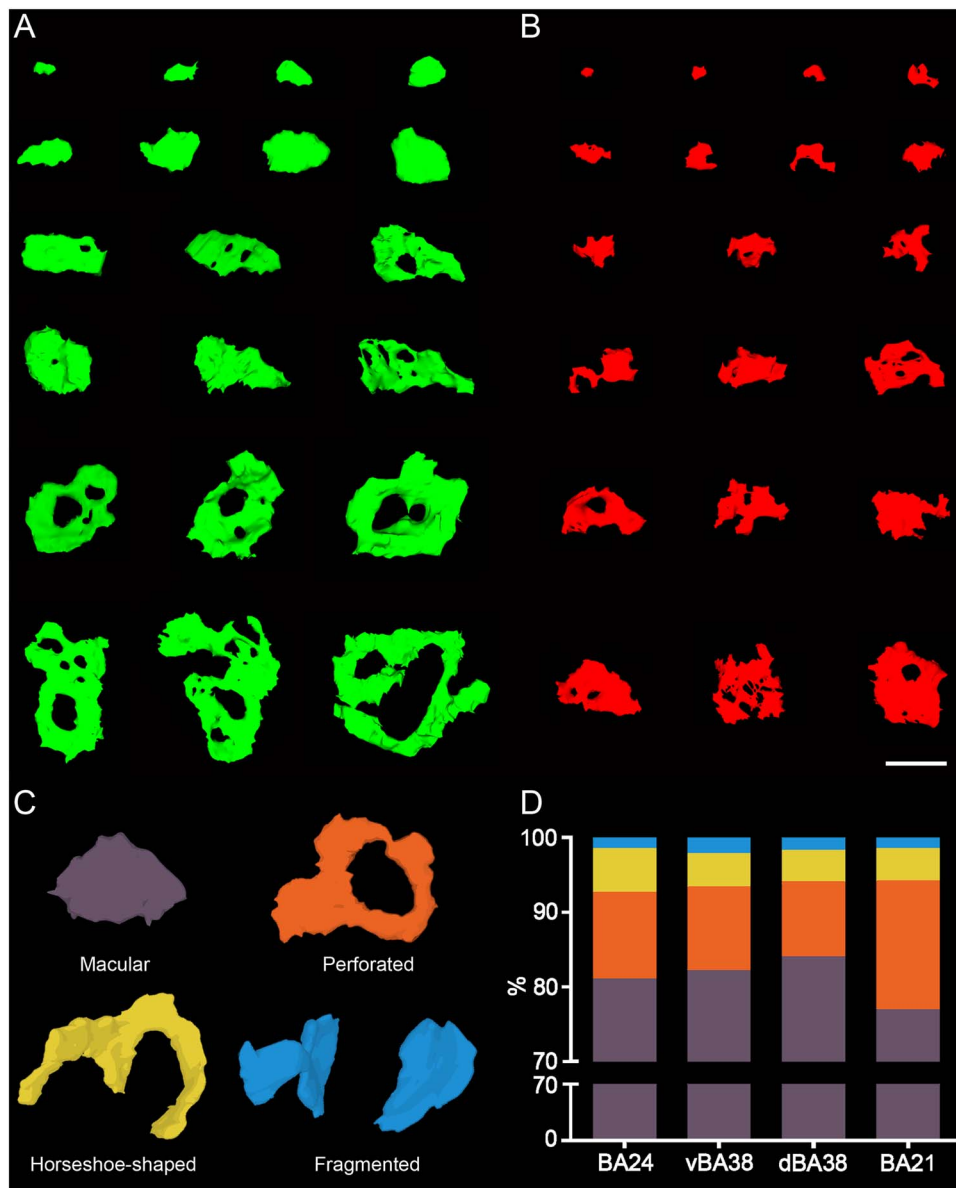


**Fig. 5.** Study of the morphology of the synapses. 3D synaptic morphology representation. (A, B) Representative examples of SAS of asymmetric synapses (A, green) and symmetric synapses (B, red). Analyses of SAS were distributed into 20 bins of equal size (an example of each bin has been illustrated). (C) Schematic representation of the shape of the synaptic junctions: macular synapses, with continuous disk-shaped PSD; perforated synapses, with holes in the PSD; horseshoe-shaped synapses, with tortuous horseshoe-shaped perimeter with an indentation; and fragmented synapses, with two or more PSDs with no connections between them. (D) Proportion of macular, perforated, horseshoe-shaped, and fragmented AS in BA24, vBA38, dBA38, and BA21. BA21 showed a higher proportion of complex-shaped synapses (including perforated, horseshoe, and fragmented synapses) than BA24, vBA38, and dBA38 ( $\chi^2$ ;  $P < 0.0001$ ). Scale bar (in B) indicates 500 nm in (A) and (B). BA: Brodmann area; d: dorsal; SAS: synaptic apposition surface; v: ventral.

with regard to the volume occupied by the cortical structures, the synaptic type, the synaptic shapes, and their postsynaptic targets. Kruskal–Wallis (KW) nonparametric test, with post-hoc correction (via Dunn's multiple comparisons) was performed to analyze the area of the SAS. Frequency distribution analysis of the SAS was performed using Kolmogorov–Smirnov (KS) nonparametric test.

Statistical studies were performed with the GraphPad Prism statistical package (Prism 9.00 for Windows, GraphPad Software Inc., USA), Spatstat package and RProject program (Baddeley et al. 2015), as well as the online tool VassarStats (<http://vassarstats.net/>).

## Results

### Volume fraction of cortical elements

Volume fraction (Vv) was estimated applying the Cavalieri principle (Gundersen et al. 1988) in layer III of BA24, vBA38, dBA38, and BA21 to determine the relative volume occupied by different cortical elements: neuropil, cell bodies (including neurons, glial cells and undetermined cells), and blood vessels. The neuropil constituted the main component in all regions (more than 80%; Fig. 2; Supplementary Table 1), followed by cell bodies (ranging from 6.80% in vBA38 to 11.88% in BA24) and blood vessels (ranging from 2.81% in BA21 to 3.75% in BA24) (Fig. 2; Supplementary Table 1).

**Table 1.** Accumulated data obtained from the ultrastructural analysis of neuropil from layer III of BA24, vBA38, dBA38, and BA21 in human autopsy samples. Data in parentheses have not been corrected for shrinkage. The data for individual cases are shown in [Supplementary Table 2](#). AS: asymmetric synapses; BA: Brodmann area; CF: counting frame; d: dorsal; SAS: synaptic apposition surface; SD: standard deviation; SE: standard error of the mean; SS: symmetric synapses; v: ventral.

	BA24	vBA38	dBA38	BA21
No. AS	1,335	1,544	2,279	1,129
No. SS	95	85	145	83
No. synapses (AS+SS)	1,430	1,629	2,424	1,212
% AS	93.21%	94.65%	93.95%	93.28%
% SS	6.79%	5.35%	6.05%	6.72%
CF volume ( $\mu\text{m}^3$ )	3,144 (2,831)	3,110 (2,801)	3,166 (2,851)	2,483 (2,236)
No. AS/ $\mu\text{m}^3$ (mean $\pm$ SD)	0.46 $\pm$ 0.06 (0.51 $\pm$ 0.06)	0.49 $\pm$ 0.09 (0.55 $\pm$ 0.10)	0.71 $\pm$ 0.11 (0.79 $\pm$ 0.13)	0.46 $\pm$ 0.06 (0.51 $\pm$ 0.07)
No. SS/ $\mu\text{m}^3$ (mean $\pm$ SD)	0.03 $\pm$ 0.01 (0.03 $\pm$ 0.01)	0.03 $\pm$ 0.00 (0.03 $\pm$ 0.00)	0.05 $\pm$ 0.01 (0.05 $\pm$ 0.01)	0.03 $\pm$ 0.01 (0.03 $\pm$ 0.01)
No. all synapses/ $\mu\text{m}^3$ (mean $\pm$ SD)	0.49 $\pm$ 0.06 (0.54 $\pm$ 0.06)	0.52 $\pm$ 0.08 (0.58 $\pm$ 0.09)	0.76 $\pm$ 0.12 (0.84 $\pm$ 0.13)	0.49 $\pm$ 0.06 (0.54 $\pm$ 0.07)
Intersynaptic distance (nm; mean $\pm$ SD)	845 $\pm$ 27 (785 $\pm$ 25)	821 $\pm$ 28 (763 $\pm$ 26)	739 $\pm$ 48 (686 $\pm$ 44)	821 $\pm$ 52 (797 $\pm$ 50)
Area of SAS AS ( $\text{nm}^2$ ; mean $\pm$ SE)	119,498 $\pm$ 2,425 (111,133 $\pm$ 2,255)	111,388 $\pm$ 2,298 (103,590 $\pm$ 2,137)	77,265 $\pm$ 1,510 (71,856 $\pm$ 1,404)	113,178 $\pm$ 2,626 (105,256 $\pm$ 2,442)
Area of SAS SS ( $\text{nm}^2$ ; mean $\pm$ SE)	67,537 $\pm$ 5,622 (62,890 $\pm$ 5,229)	55,084 $\pm$ 3,892 (51,228 $\pm$ 3,620)	52,460 $\pm$ 2,688 (48,788 $\pm$ 2,500)	62,469 $\pm$ 5,342 (58,096 $\pm$ 4,968)

The volume occupied by cell bodies was significantly higher in BA24 than in any other region ( $\chi^2$ ,  $P < 0.001$ ; BA24: 11.88%; vBA38: 6.80%; dBA38: 8.09%; BA21: 8.76%).

## Synaptic density

To study the synaptic organization of BA24, vBA38, dBA38, and BA21 across different human cases, their synapses were studied in the 34 stacks of images obtained in the layer III neuropil (i.e. excluding cell bodies, blood vessels, and major dendritic trunks).

A total of 2,052, 1,801, 3,230, and 1,676 synaptic junctions were individually identified and 3D reconstructed in BA24, vBA38, dBA38, and BA21, respectively. Of these, 1,430 (BA24), 1,629 (BA38), 2,424 (dBA38), and 1,212 (BA21) synapses were analyzed after discarding incomplete synapses or those touching the exclusion edges of the counting frame (CF; see below) (Table 1; [Supplementary Table 2](#)). The synaptic density data were obtained by dividing the total number of synapses included within the CF by its inclusion volume. The synaptic density analyses performed in the neuropil of layer IIIA revealed a very narrow range of values for the number of synapses per volume in all cases and regions analyzed: 0.43–0.55 synapses/ $\mu\text{m}^3$  in BA24, 0.47–0.62 synapses/ $\mu\text{m}^3$  in vBA38, 0.65–0.89 synapses/ $\mu\text{m}^3$  in dBA38, and 0.44–0.51 synapses/ $\mu\text{m}^3$  in BA21 (Table 1; [Supplementary Table 2](#)). The mean synaptic density values obtained in dBA38 were significantly higher (ANOVA;  $P < 0.05$ ) than those obtained in BA24, vBA38, and BA21 (Fig. 6).

The proportions of AS and SS were also calculated for all samples. As shown in Table 1 (see also [Supplementary Table 2](#)), the proportion of AS:SS was 93:7 in BA24 and BA21, 95:5 in vBA38, and 94:6 in dBA38. No differences were observed in the AS:SS proportion between regions ( $\chi^2$ ;  $P > 0.05$ ).

## Three-dimensional spatial synaptic distribution

To analyze the spatial distribution of the synapses, the actual position of each of the synaptic junctions in each stack of images was compared with the Complete Spatial Randomness (CSR) model. For this, the functions G, K, and F were calculated in the 34 stacks of images analyzed in BA24, vBA38, dBA38, and BA21. We found that six stacks of images did not fit into the CSR model, showing a slight tendency for a regular pattern in at least one of

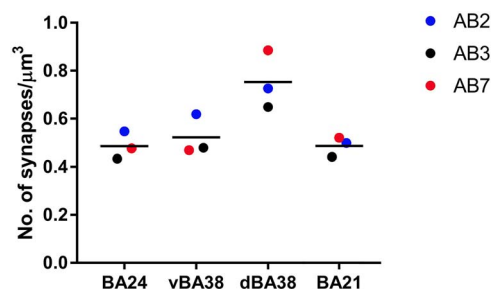


**Fig. 6.** Synaptic density. Mean synaptic density of the neuropil from layer III of BA21, BA24, vBA38, and dBA38. Each dot represents a single autopsy case according to the colored key on the right. dBA38 shows a significantly higher synaptic density than the other analyzed regions (ANOVA;  $P < 0.05$ ). BA: Brodmann area; d: dorsal; v: ventral.

the functions ([Supplementary Fig. 2A](#)). In the remaining samples (i.e. 28 out of 34 stacks), the three spatial statistical functions resembled the theoretical curve that simulates the random spatial distribution pattern, which indicated that synapses fitted a random spatial distribution model in all areas examined (BA24, BA38v, dBA38d, and BA21) ([Supplementary Fig. 2B](#)).

In addition, the mean distance of each synaptic junction centroid to its nearest neighboring synaptic junction was estimated. The analysis showed that the distance to the nearest neighboring synapse in dBA38 was smaller than in the other cortical areas—differences that were statistically different (KW;  $P < 0.01$ ) compared with BA24 (Table 1; [Supplementary Table 2](#)). No significant differences were found between the remaining cortical areas.

## Study of the morphology of the synapses

### Synaptic size

The study of the synaptic size was carried out analyzing the area of the synaptic apposition surface (SAS) of each synaptic junction identified and 3D reconstructed in all FIB/SEM stacks. As shown in [Fig. 5\(A, B\)](#), the size and shape of the SAS were rather variable. The average size of the synapses (measured by the area of the SAS) showed that AS were statistically larger than SS in all regions (Table 1; [Supplementary Table 2](#)). To characterize the data distribution of AS and SS SAS area, we performed goodness-of-fit



tests to find the theoretical probability density functions that best fitted the empirical distributions of SAS areas in all regions. We found that the best fit corresponded to log-normal distributions, with some variations in the location ( $\mu$ ; range: 10.888–11.413 in AS and 10.673–10.820 in SS) and scale ( $\sigma$ ; range: 0.7872–0.8690 in AS and 0.6499–0.8091 in SS) parameters. This was the case in all regions for both AS and SS, although the fit was better for AS than for SS, probably due to the smaller number of SS.

Comparison of the probability density functions between AS and SS showed that larger synaptic junctions were more frequent in AS than SS in all regions (KS;  $P < 0.001$ ; [Supplementary Fig. 3](#)). Upon the analyses of the average area of the SAS of AS between cortical regions, significant differences (KW;  $P < 0.0001$ ) were found between regions, indicating that AS were smaller in dBA38 than in vBA38, BA24, and BA21. Also, significant differences (KW;  $P < 0.05$ ) were found between the mean SAS area of AS in vBA38 and BA24, indicating that AS in vBA38 were smaller than in BA24 ([Table 1](#); [Supplementary Table 2](#)). Similarly, significant differences were found when comparing the AS SAS area frequency distribution between cortical regions, indicating that smaller AS were more frequent in dBA38 than vBA38, BA24, and BA21 (KS,  $P < 0.0001$ ). Furthermore, smaller AS were more frequent in vBA38 than BA24 (KS,  $P = 0.0004$ ). The number of SS examined in all areas was not sufficient to perform a robust statistical analysis focusing on possible differences between SAS in different regions.

### Synaptic shape

To analyze the shape of the synaptic contacts, we classified each identified synapse into four categories: macular (with a flat, disk-shaped PSD), perforated (with one or more holes in the PSD), horseshoe (with an indentation in the perimeter of the PSD), or fragmented (with two or more physically discontinuous PSDs) ([Fig. 5C](#); for a detailed description, see [Santuy et al. 2018a](#); [Domínguez-Álvarez et al. 2019](#)). The analyses showed that the vast majority of AS presented macular shape in all of the cortical regions analyzed (range: 77–84%), followed by perforated (range: 10–17%), horseshoe (range: 4–6%) and fragmented (range: 1–2%; [Supplementary Table 3](#)). Regarding the SS, the results were very similar in all analyzed regions: the majority of SS presented a macular shape (range: 85–92%; [Supplementary Table 3](#)), whereas the perforated (range: 2–8%) and horseshoe (range: 2–6%) shapes were less frequent. SS exhibiting a fragmented shape were scarce; indeed, this shape was only identified in three synapses in vBA38, 1 synapse in dBA38 and 1 synapse in BA21 ([Supplementary Table 3](#)).

To determine whether there was a difference in the proportion of AS shapes between regions, contingency tests were applied. Perforated, horseshoe, and fragmented synapses were computed as a whole (as complex-shaped synapses), and statistically significant differences were found ( $\chi^2$ ,  $P < 0.0001$ ) indicating that complex-shaped AS were more frequent in BA21 (33.0%) than in vBA38 (17.8%), dBA38 (15.9%), and BA24 (18.8%) ([Fig. 5D](#); [Supplementary Table 3](#)). Concerning SS, the number of synapses was not sufficient to perform a robust statistical analysis to analyze possible differences between cortical areas.

### Synaptic size and shape

We also determined whether the shape of a synapse is related to its size. For this purpose, the areas of the SAS—AS and SS—were analyzed according to the synaptic shape. We found that the area of the macular AS was smaller (KW;  $P < 0.0001$ ) than the area of the perforated, horseshoe, and fragmented AS in all regions ([Supplementary Table 4](#)). Similarly, the smaller AS were

more frequent in the macular-shaped synapses in all cortical regions (KS;  $P < 0.0001$ ; [Supplementary Fig. 4](#)). SS numbers were not sufficient to perform a robust statistical analysis.

### Study of the postsynaptic targets

Postsynaptic targets were identified and classified as spines (axospinous synapses) or dendritic shafts (axodendritic synapses). We also determined whether the synapse was located on the neck or head of a spine ([Fig. 7](#)).

When the postsynaptic element was identified as a dendritic shaft, it was classified as “with spines” or “without spines” ([Supplementary Table 5](#)). The postsynaptic elements of 1,262, 1,574, 2,350, and 1,143 synapses were determined in BA24, vBA38, dBA38, and BA21, respectively. In all analyzed cortical regions, most synapses were AS established on spine heads (range: 68.5–73.4%) followed by AS on dendritic shafts (range: 20.8–24.0%), SS on dendritic shafts (range: 3.7–5.7%) and AS on spine necks (range: 0.6–1.1%) ([Fig. 5](#)). The least frequent types of synapses were SS established on spine heads (range: 0.8–1.3%) and SS on spine necks (range: 0.3–0.5%) ([Fig. 8](#)).

Comparisons of the AS postsynaptic targets between cortical regions were analyzed and no differences were found ( $\chi^2$ ,  $P > 0.05$ ; [Supplementary Table 5](#)). Concerning SS, the number of synapses examined was not sufficient to perform a robust statistical analysis.

In addition, to detect the presence of multiple synapses, an analysis of the spine heads was performed to determine the number and type of synapses established on them. The vast majority of spines had a single AS (range: 93–96%) followed by spines with a large variety in the synapse number and location (head or neck) of AS and SS ([Fig. 9](#)). A comparison of the multisynaptic spine proportions between cortical regions was also carried out. Spines with more than one AS ([Fig. 9](#)) were significantly more frequent in BA24 than in the other regions ( $\chi^2$ ,  $P < 0.05$ ).

### Postsynaptic targets and synaptic size

Finally, we also determined whether the postsynaptic elements of the synapses were related to their size. For this purpose, the areas of the SAS—of both AS and SS—were analyzed according to the postsynaptic targets. In order to perform a more accurate analysis of the size of the axospinous synapses, we excluded those synapses established on incomplete spines. Large AS were more frequently found on spines than on dendritic shafts (with and without spines) in all regions (KS;  $P < 0.01$ ; [Supplementary Fig. 5](#)).

The area of the AS established on spines was significantly larger than the area of the AS established on different targets depending on the region (KW;  $P < 0.01$ ; [Supplementary Table 6](#)). The number of SS analyzed was not sufficient to perform a robust statistical analysis.

### Synaptic interindividual variability

We also studied the variability between individuals. As shown in [Supplementary Table 2](#), the synaptic density found in the three cases in dBA38 was more variable (0.65–0.89 synapses/ $\mu\text{m}^3$ ) than in any other cortical region, especially when comparing to BA21, where the synaptic density of the three cases were remarkably similar (0.44–0.51 synapses/ $\mu\text{m}^3$ ). In the case of dBA38, the percentage of macular synapses was between 83 and 94%, which is higher than any other cortical region and, again, notably higher than in BA21 where the macular synapse percentages were very similar (75.9–77.6%; [Supplementary Table 3](#)) in the three cases. Finally, in BA21 the percentage of AS established on spine heads varied depending on the case: 67, 71, and 82% in cases AB3, AB2,

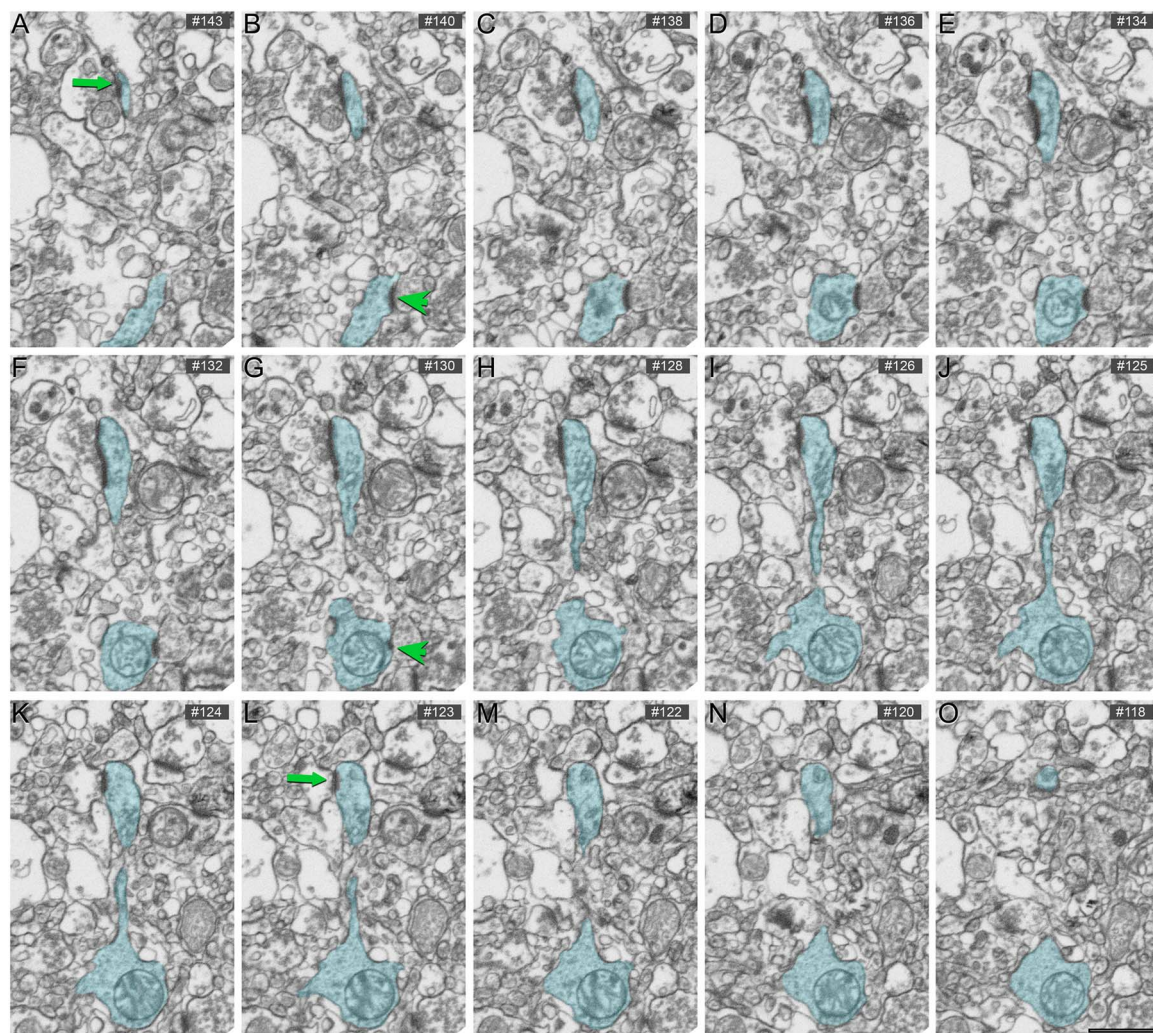


**Fig. 7.** Serial images obtained by FIB/SEM showing a dendritic segment with a spine (blue). Asymmetric synapses established on the spine head (green arrow; A–L) and the dendritic shaft (green arrowhead; B–G) are indicated. Scale bar (in O) = 1  $\mu$ m.

and AB7, respectively. However, in BA24, the percentages for the three cases were very similar (71–74%; [Supplementary Table 5](#)).

## Discussion

The present results provide a large quantitative ultrastructural dataset of synapses in layer III of the anterior cingulate and temporopolar cortex using 3D EM. The main result is that there were synaptic characteristics specific to particular regions (synaptic density and synaptic size were different in dBA38), whereas some other synaptic characteristics were common to all analyzed regions, including (i) a similar AS:SS ratio; (ii) synapses fitted into a random spatial distribution; (iii) the SAS area of AS was larger than that of SS; (iv) most synapses displayed a macular shape, and they were smaller than complex-shaped synapses; (v) most synapses were AS established on spines, followed by AS on dendritic shafts and SS on dendritic shafts; (vi) AS on spine heads were larger than AS on dendritic shafts; and (vii) most spine heads receive a single AS.

## Synaptic density

3D EM synaptic datasets allow the direct counting of synaptic junctions, which is a much less variable method of quantification than stereological ones, so the resulting datasets can be

considered more robust than those coming from conventional EM. Moreover, it is difficult to reliably compare measurements obtained from the 3D EM datasets with those obtained from TEM (for a detailed description see [Rollenhagen et al. 2020](#); [Cano-Astorga et al. 2021](#) and references therein). Thus, our discussion on synaptic organization only includes datasets coming from 3D EM technologies.

Most connections in the cerebral cortex are established by point-to-point chemical synapses ([DeFelipe 2015](#)). Therefore, determining the synaptic density in a given region is important since this parameter is crucial in terms of connectivity and functionality. In the present study, we found that the mean synaptic density of the neuropil of layer III in dBA38 (0.79 synapses/ $\mu$ m<sup>3</sup>) was significantly higher than in BA24 (0.49 synapses/ $\mu$ m<sup>3</sup>), BA21 (0.49 synapses/ $\mu$ m<sup>3</sup>), and vBA38 (0.52 synapses/ $\mu$ m<sup>3</sup>). Previous studies using the same techniques (in the same autopsy cases, AB2 and AB3) have shown that the synaptic density in the neuropil of other cortical regions—such as layer II of the transentorhinal cortex ([Domínguez-Álvarez et al. 2018](#)) and layers II and III of the entorhinal cortex ([Domínguez-Álvarez et al. 2021a](#))—were similar to the synaptic density of BA24, BA21, and vBA38 found in the present study. However, in the deep and superficial stratum pyramidale of the *Cornu Ammonis* 1 (CA1) field of the hippocampus of these autopsy cases, the





**Fig. 8.** Study of the postsynaptic targets. Schematic representation of the asymmetric and symmetric synapses on the different postsynaptic targets (spine head, spine neck and dendritic shaft) from analyzed synapses in layer III of BA24 (A), vBA38 (B), dBA38 (C), and BA21 (D). Spine head percentages include both complete and incomplete spines. Dendritic shaft percentages include dendritic shafts with and without spines. No significant differences ( $\chi^2$ ;  $P > 0.05$ ) were found between cortical regions. AS have been represented in green and SS in red. BA: Brodmann area; d: dorsal; v: ventral.

synaptic density was 0.67 and 0.99 synapses/ $\mu\text{m}^3$ , respectively (Montero-Crespo et al. 2020), which is closer to the synaptic density found in dBA38. As the tissue processing and analysis methods were identical, similarities and differences would appear to be attributable to specific characteristics of the brain region and layer analyzed.

The proportion of tissue occupied by neuropil (Vv-neuropil) is clearly also an important factor in terms of synaptic connectivity of the cortical region and layer. In the present study, the Vv-neuropil constituted the main component of layer III of BA24, vBA38, dBA38, and BA21 (range: 84–90%). These were similar values to those obtained in the same autopsy cases in layer II of the human transentorhinal cortex (Domínguez-Álvarez et al. 2018) and in the pyramidal cell layer of the CA1 field of the hippocampus (Montero-Crespo et al. 2020).

These apparently small differences in the Vv-neuropil, however, could imply substantial differences in the overall number of synapses (DeFelipe et al. 1999). As in the present study we found that the synaptic density varies within a range of between approximately 0.5 and 0.8 synapses per  $\mu\text{m}^3$ , both the density and the Vv-neuropil should be considered together. For example, BA24 had a lower Vv-neuropil (84%) than BA21 (88%), dBA38 (89%), and vBA38 (90%). However, the synaptic density of BA24 was similar to BA21 and vBA38, but much lower than in dBA38. Hence, considering the synaptic density and the Vv-neuropil together, layer III of BA24 must contain a lower number of synapses than the other regions. Thus, the significance of volume fraction variations must be considered together with the synaptic density and the total volume of the layer to better understand the overall connectivity of these cortical regions.

Moreover, the present results regarding synaptic density are in line with the higher spine density and pyramidal complexity reported in layer III from BA38 (Benavides-Piccione et al. 2013, 2021). These studies focusing on human pyramidal neurons have shown that in the BA38, pyramidal neurons had higher branching complexity and higher spine density than in BA21 and BA24 (Benavides-Piccione et al. 2021). In addition, both BA38 and BA21 had higher spine densities than BA24 (Benavides-Piccione et al. 2013). As pyramidal neurons represent the majority of cortical neurons and their spines are the major target of AS, a direct correlation between synaptic density and complexity of pyramidal neurons may exist. Further studies would be needed to investigate the possible correlation of spine density and synaptic density in other cortical areas.

### Proportion of synapses and spatial synaptic distribution

It is well established that the cortical neuropil has a larger proportion of AS than SS regardless of the cortical region and species (rodent, monkey or human). Using transmission electron microscopy, this proportion varies between 80 and 95% for AS and 20–5% for SS (reviewed in DeFelipe et al. 2002; DeFelipe 2011; for a recent study see Cano-Astorga et al. 2021 and references therein). Similar proportions have been found using FIB/SEM in the present study and in other cortical regions (Domínguez-Álvarez et al. 2018, 2021a; Montero-Crespo et al. 2020; Cano-Astorga et al. 2021). Therefore, regarding the proportion of AS and SS in the human cerebral cortex, it seems that the values are among the highest for AS and among the lowest for SS in the mammalian cerebral cortex.

The significance of this similar AS:SS ratio is difficult to interpret due to the differences in the cytoarchitecture, connectivity, and functional characteristics of different brain regions. A variety of neurochemical and functional types of pyramidal and GABAergic neurons are present in these regions but their densities vary. For example, the human cingulate cortex (BA24) contains more immunoreactive interneurons for tyrosine-hydroxylase than the temporal cortex (including BA21 and BA38; Benavides-Piccione et al. 2005; Benavides-Piccione and DeFelipe 2007), whereas the human temporal pole cortex (BA38) has more immunoreactive interneurons for parvalbumin than BA21 and BA24 (Blázquez-Llorca et al. 2010).

One possibility is that the AS:SS ratio in the dendritic arbor of the different types of neurons may be similar. However, in other cortical regions of different species, it has been shown that there are differences in the number of GABAergic and glutamatergic inputs in several neuronal types (e.g. DeFelipe and Fariñas 1992; Freund and Buzsáki 1996; DeFelipe 1997; Somogyi et al. 1998; Schubert et al. 2007; Markram et al. 2015; Tremblay et al. 2016; Hu and Vervaeke 2018; Sohal and Rubenstein 2019; Chini et al. 2022).

Thus, it would be necessary to examine the synaptic inputs of each particular cell type to determine differences in their AS:SS ratio, even though the overall AS:SS proportion does not vary in the neuropil. Finally, we would like to point out that we have focused on the synaptic organization of the neuropil, leaving aside the perisomatic innervation—the study of which is also critical to better understand the synaptic organization of cortical circuits (for a recent study, see Ostos et al. 2023). The reason for this is that our FIB/SEM stacks of images may include axo-axonic synapses by chance, but, as these synapses are very infrequent, random sampling of FIB/SEM stacks in the neuropil would not be the best strategy. Moreover, the study of the axo-somatic synapses on

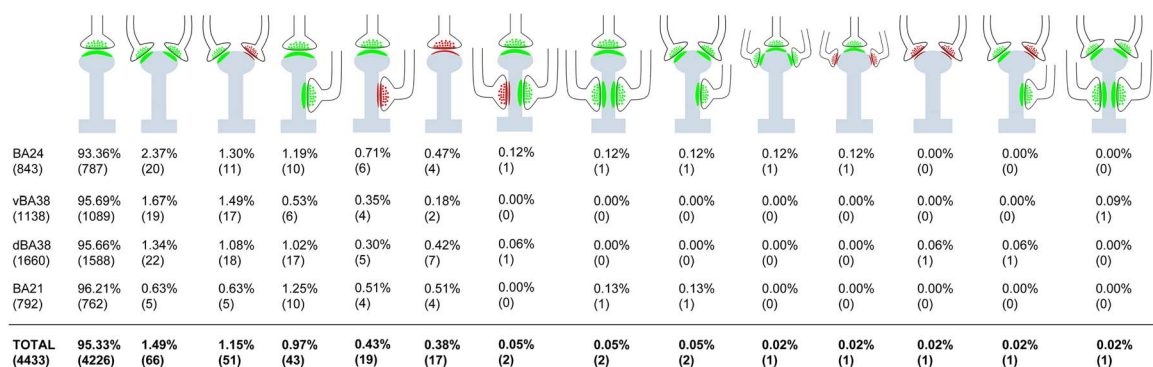


**Fig. 9.** Study of the postsynaptic targets-multisynaptic spines. Schematic representation of spine heads (including both complete and incomplete spines) receiving single and multiple synapses in BA24, vBA38, dBA38, and BA21. Percentages of each type are indicated (absolute numbers of synapses are in parentheses). AS have been represented in green and SS in red. Spines with more than one AS (including all combinations) were more frequent in BA24 than in the other regions ( $\chi^2$ ,  $P < 0.05$ ). AS: asymmetric synapses; BA: Brodmann area; d: dorsal; SS: symmetric synapses; v: ventral.

pyramidal cells would require a different technical approach. As cell somata are large structures, particularly in relation to the high magnification of EM necessary to identify the synapses, a soma may occupy a significant part (if not all) of any EM image and there would clearly be very few—if any—synapses to be analyzed. Thus, we are planning to analyze both axo-axonic and axo-somatic synapses in the near future using different technical approaches.

The analysis of the spatial organization of synapses showed that the synapses were randomly distributed in the neuropil from most of the samples of BA24, vBA38, dBA38, and BA21. This spatial distribution has also been found in other regions of the human brain, including transentorhinal and entorhinal cortex, and CA1 field of the hippocampus (Domínguez-Álvarez et al. 2018, 2021a; Montero-Crespo et al. 2020). Therefore, the present results—regarding the AS:SS proportion and spatial distribution of synapses—support the idea that the synaptic organization of the human cerebral cortex follows general rules.

## Synaptic size and shape

It has been proposed that synaptic size correlates with release probability, synaptic strength, efficacy, and plasticity (see Chindemi et al. 2022 and references therein). Several methods have traditionally been used to estimate the size of synaptic junctions making it difficult to compare between different studies (reviewed in Cano-Astorga et al. 2021). In addition, most studies estimate the size of synapses in general (mostly AS) but few reports provide specific data regarding the size of the SS. Here, we have found that AS were larger than SS in all the regions analyzed, as previously reported in other human cortical regions such as layer II of the transentorhinal cortex (Domínguez-Álvarez et al. 2018), layers II and III of the entorhinal cortex (Domínguez-Álvarez et al. 2021a), and in all layers of the CA1 field of the hippocampus (Montero-Crespo et al. 2020). Using the same techniques in other mammalian species, AS were also found to be larger than SS in all layers of the somatosensory cortex of the Etruscan Shrew (Alonso-Nanclares et al. 2023) and juvenile rat (Santuy et al. 2018a). However, it has been shown that SS were larger than AS in certain layers of the CA1 field of the mouse hippocampus and in certain layers of the mouse somatosensory cortex (Santuy et al. 2020; Turégano-López et al. 2022). Thus, further studies should be performed in other cortical areas, layers, and species to find out if this characteristic is a regional and/or species-specific rule of the mammalian cerebral cortex.

Additionally, the pool of synaptic vesicles correlates with synaptic transmission and plasticity (reviewed in Rizzoli and

Betz 2005). Thus, studies based on positron emission tomography combined with magnetic resonance imaging have used the pool of synaptic vesicles as a marker of synaptic density and function, in both healthy and pathological human individuals (Finnema et al. 2016; Chen et al. 2018; Onwordi et al. 2020; Radhakrishnan et al. 2021). However, assessment of the pool of synaptic vesicles presents a variety of spatiotemporal challenges: changes in the pool of synaptic vesicles are fast (Matz et al., 2010), the synaptic vesicle distribution within the axonal terminal has different functional implications (Rizzoli and Betz 2005), and the changes in the pool of synaptic vesicles of a given axonal terminal trigger particular point-to-point changes in other axonal terminals in distant cortical regions (Felleman and Van Essen 1991). Therefore, care should be taken when interpreting the functional implications of the changes in the pool of synaptic vesicles. To better understand these changes, several ultrastructural studies have characterized the size and distribution of the pool of synaptic vesicles within individual axonal terminals in a variety of mammalian species, including humans (Yakoubi et al. 2019a, 2019b; Schmuhl-Giesen et al. 2022). Thus, the systematic ultrastructural characterization of the size and distribution of the synaptic vesicle pools in different cortical layers and regions could improve our understanding about the functional implications of the in vivo recording of the synaptic vesicle pool's changes.

In addition, the densities of N-methyl-D-aspartate (NMDA), kainate, and norepinephrine receptors have been reported to be higher in BA24 than in BA38 (Palomero-Gallagher et al. 2008; Zilles and Palomero-Gallagher 2017). This seems to be in contrast with our results since synaptic density in BA24 was lower than in dBA38. Synaptic size is related to the number of receptors in the PSD—larger PSD have a larger number of receptors (reviewed in Lüscher et al. 2000; Lüscher and Malenka 2012; Toni et al. 2001; Magee and Grienberger 2020; Sumi and Harada 2020). In particular, BA24 had the largest AS compared with the other regions examined. Nevertheless, the above-mentioned receptors have been reported to be synaptically and extra-synaptically located depending on each receptor (Palomero-Gallagher and Zilles 2019). Therefore, caution should be taken regarding possible correlations between receptor densities, number of synapses and/or synaptic size. Indeed, the differences and similarities in the synaptic density between human cortical regions—as well as the particular regional densities of receptors of various neurotransmitters—should be considered together to better understand the functional organization of synaptic circuits.



Analysis of the AS SAS area revealed that BA24, BA21 and vBA38 had similar values ( $\sim 110,000$  to  $\sim 120,000$  nm<sup>2</sup>) to those obtained in layer II of the transentorhinal cortex (Domínguez-Álvarez et al. 2018) and layers II and III of the entorhinal cortex (Domínguez-Álvarez et al. 2021a). In the case of dBA38, the mean SAS area of AS was  $\sim 80,000$  nm<sup>2</sup>, which was different from the above-mentioned regions but was similar to those obtained in all layers of the CA1 field of the hippocampus (Montero-Crespo et al. 2020). Using PSD manual tracing (which is a 3D method of measuring synaptic size comparable with SAS), it has been reported that the mean synaptic size in the layer IV of the human temporal neocortex was  $\sim 130,000$  nm<sup>2</sup> (Yakoubi et al. 2019b)—similar to the present results obtained in BA24, vBA38, and BA21. In the case of layers VI and V of the human temporal neocortex, the mean synaptic size was reported to be higher ( $\sim 180,000$  nm<sup>2</sup>; Schmuhl-Giesen et al. 2022) and much higher ( $\sim 270,000$  nm<sup>2</sup>; Yakoubi et al. 2019a), respectively, than in any other human cortical region measured by 3D morphological methods (Domínguez-Álvarez et al. 2018, 2021a; Yakoubi et al. 2019b; Montero-Crespo et al. 2020; and the present results). This difference in the reported synaptic size could be related to particularities of layer V and VI, which, as far as we know, have not been measured in 3D EM previously. However, the results of Yakoubi et al. (2019a), Schmuhl-Giesen et al. (2022), and Yakoubi et al. (2019b) come from the analyses of 120, 147, and 155 reconstructed synaptic junctions, respectively. Thus, the differences found between layers V and VI of the temporal neocortex and those obtained in the supragranular layers of other human cortical regions (Domínguez-Álvarez et al. 2018, 2021a; Yakoubi et al. 2019b; Montero-Crespo et al. 2020; and the present results) could be related to the relatively small number of synapses analyzed. Therefore, large 3D morphological datasets collected in layers V and VI could help to further elucidate the synaptic morphology of these layers.

Analysis of the SS SAS area showed no differences between the cortical regions analyzed in the present study and other human cortical regions analyzed by 3D EM (52,000–67,000 nm<sup>2</sup>; Domínguez-Álvarez et al. 2018, 2021a; Montero-Crespo et al. 2020; the present study). Thus, the SS seem to constitute a more homogeneous population of synapses than AS in this regard.

Furthermore, we found that most synapses presented a macular shape (81–85%), whereas 15–19% were complex-shaped synapses (including perforated, horseshoe, and fragmented)—with complex-shaped AS being larger than macular AS. These observations are comparable with previous reports in other brain areas and species (Geinisman et al. 1987; Jones et al. 1991; Neuman et al. 2016; Hsu et al. 2017; Cali et al. 2018; Santuy et al. 2018a; Domínguez-Álvarez et al. 2019, 2021a; Montero-Crespo et al. 2020; Cano-Astorga et al. 2021). It has been reported that complex-shaped synapses have more  $\alpha$ -amino-3-hydroxy-5-methyl-4-isoxazolepropionic acid (AMPA) and NMDA receptors than macular synapses, and they are thought to constitute a relatively “powerful” population of synapses with more long-lasting memory-related functionality than macular synapses (Geinisman et al. 1987, 1991, 1992a, 1992b, 1993; Lüscher et al. 2000; Toni et al. 2001; Ganeshina et al. 2004a, 2004b; Spruston 2008). Thus, determining the shape of synapses is interesting from the functional point of view. The proportion of complex-shaped synapses was higher in BA21 than in the other analyzed regions. In particular, dBA38 had the lowest proportion of complex-shaped synapses. Thus, dBA38 seems to display a variety of distinct synaptic characteristics compared with vBA38, BA21, and BA24, including high synaptic density, small synaptic size (SAS area), and a low proportion of complex-shaped synapses.

## Postsynaptic targets

A clear preference of glutamatergic axons (forming AS) for spines, and GABAergic axons (forming SS) for dendritic shafts, was observed (Fig. 8). This is in line with the numerous studies using electron microscopy in a variety of cortical regions and species (reviewed in DeFelipe et al. 2002). However, this characteristic is commonly misinterpreted as implying that synapses on shafts are mostly SS. In fact, this is not the case—quantitative analyses of synapses in the neuropil have shown that most synapses are AS established on spines, followed by AS on dendritic shafts, and then SS on dendritic shafts (Beaulieu et al. 1992; Peters et al. 2008; Hsu et al. 2017; Cali et al. 2018; Santuy et al. 2018b; Domínguez-Álvarez et al. 2019, 2021a, 2021b; Yakoubi et al. 2019b; Montero-Crespo et al. 2020, 2021; Cano-Astorga et al. 2021).

In the present study, the simultaneous analysis of the synaptic type and postsynaptic target showed that the proportions of AS on spines (“axospinous”) were around 73–77%. Using the same FIB/SEM technology in other cortical regions in the same autopsy samples (AB2 and AB3), the proportions of AS established on spines were similar in layer II of the human transentorhinal cortex (75%; Domínguez-Álvarez et al. 2021a) and stratum oriens, deep stratum pyramidale, and stratum radiatum of the CA1 hippocampal field (77–81%; Montero-Crespo et al. 2020). However, this percentage was much lower in layers II and III of the human entorhinal cortex (60 and 56%, respectively; Domínguez-Álvarez et al. 2021a) and in the stratum lacunosum-moleculare of the CA1 hippocampal field (57%; Montero-Crespo et al. 2020). The superficial stratum pyramidale of the CA1 hippocampal field had a higher proportion of AS established on spines (88%; Montero-Crespo et al. 2020). Therefore, these peculiarities in the proportion of AS on spines and dendritic shafts represent another microanatomical specialization of the cortical regions (and layers) examined, which may have important functional implications in the processing of information of these cortical regions.

In addition, we found that AS established on spine heads were larger than those established on dendritic shafts or spine necks, as was previously reported in layer II of the transentorhinal cortex (Domínguez-Álvarez et al. 2019) and layer II and III of the entorhinal cortex (Domínguez-Álvarez et al. 2021a). However, in the CA1 field of the hippocampus, no differences were found between the axospinous and axodendritic synaptic sizes (Montero-Crespo et al. 2020). Again, this suggests another regional synaptic specialization.

Regarding the number of synapses per spine, most spines established a single AS (Fig. 9), which is similar to layer II of the transentorhinal cortex (94.5%; Domínguez-Álvarez et al. 2019). However, this percentage was lower in layers II and III of the entorhinal cortex (90.3 and 89.6%, respectively; Domínguez-Álvarez et al. 2021a) and higher in the CA1 field of the hippocampus (97.7%; Montero-Crespo et al. 2020). Thus, these differences and similarities in the proportion of spines establishing single or multiple synapses between cortical regions could indicate another specialization feature of the human cerebral cortex.

The functional relevance of the presence of single/multiple synapses on the same spine remains to be elucidated. In the mice neocortex, it has been proposed that spines receiving one AS and one SS are electrically more stable than spines establishing a single AS (Villa et al. 2016). Furthermore, it has been proposed that SS may play a key role in spine calcium signaling (Chiu et al. 2013; Kleinjan et al. 2023). Since the vast majority of spines are single innervated spines, it is possible that multisynaptic spines represent a special postsynaptic target. For example, in the monkey and human cerebral cortex, it has been shown that

a particular type of GABAergic cell (forming SS), called double bouquet cells, made up around 38–48% of synapses on spines that receive additional AS (Somogyi and Cowey 1981; DeFelipe et al. 1989, 1990; de Lima and Morrison 1989; del Río and DeFelipe 1995; Lukacs et al. 2022). This is a remarkable high percentage of SS made on spines considering that dual innervated spines represent only 1–2% of the total population of synapses found in the neuropil.

## Synaptic organization and connectivity

As layer III is particularly relevant regarding cortico-cortical circuits (Felleman and Van Essen 1991; Thomson and Lamy 2007; Barbas 2015; D'Souza and Burkhalter 2017; Rockland 2019), the differences in synaptic characteristics between BA24, vBA38, dBA38, and BA21 may be related to the diversity of cortical circuits in these regions (Supplementary Fig. 6). For example, it has been described that the posterior cingulate cortex and the dorsolateral prefrontal cortex constitute a major input to BA24, vBA38, and BA21, but not to dBA38 (Pascual et al. 2015; Jackson et al. 2016; Dezachyo et al. 2021). In addition, vBA38 and dBA38 share inputs that are absent in BA24 and BA21, such as those coming from the orbital prefrontal cortex, ventrolateral prefrontal cortex and the supramarginal gyrus. BA24 and BA21, on the other hand, receive inputs from the insular cortex, which are absent in vBA38 and dBA38 (Pascual et al. 2015; Jackson et al. 2016; Dezachyo et al. 2021). Moreover, each region is characterized by the selectivity of their inputs: BA24 preferably receives inputs from the primary motor cortex and the parietal operculum cortex; vBA38 preferably receives inputs from the medial prefrontal cortex, hippocampal formation, posterior parahippocampal region, entorhinal and perirhinal cortex, and fusiform gyrus; and dBA38 preferably receives inputs from the anterior cingulate cortex, superior temporal gyrus and the neighboring areas of the Heschl's gyrus and postcentral gyrus (Pascual et al. 2015; Jackson et al. 2016; Dezachyo et al. 2021). In addition, as illustrated in Supplementary Fig. 6, there are differences in the interhemispheric connectivity in the analyzed regions. It has been proposed that there are hemispheric preferences regarding the high-order functions of the cerebral cortex, especially in humans (Bartolomeo and Seidel 2019). It has been reported that the connectivity of vBA38 and dBA38 mainly occurs in the ipsilateral hemisphere, whereas BA24 and BA21 showed a more bilateral connectivity pattern (Pascual et al. 2015; Jackson et al. 2016; Dezachyo et al. 2021). Thus, differences found regarding synaptic organization between BA24, vBA38, dBA38, and BA21 may be related to the structural and functional differences of the regions connected with them (for a detailed description, see Zachlod et al. 2022 and references therein).

Furthermore, functional and structural connectivity studies on human brain have proposed that the anterior cingulate (BA24), the temporal pole (BA38) and the middle temporal (BA21) cortices are equally connected nodes (Sporns and Zwi 2004; Sporns et al. 2005; Van Essen et al. 2013; Paquola et al. 2020). However, our present results show a differential synaptic organization in these regions, especially in terms of the synaptic density and synaptic size (see above) of excitatory synapses (which are by far the most common type of synapses involved in corticocortical connections). Nevertheless, comparing connectivity studies with our ultrastructural data is rather difficult since we have focused on layer III neuropil. That is, our results on the synaptic connectivity are restricted to dendritic shafts and spines of this particular layer of the selected cortical regions, whereas other cortical layers also receive cortico-cortical connections (Felleman and Van Essen 1991; Barbas 2015;

Rockland 2019). Furthermore, other fundamental aspects of the synaptic circuitry should be considered to decipher the relationship between local synaptic organization and functional and anatomical connectivity between cortical areas. For example, corticocortical axons innervate both excitatory and inhibitory neurons but there are variations in the types and proportions of these neurons. In addition, the perisomatic GABAergic innervation of pyramidal cells (i.e. innervation of the proximal dendrites, soma and axon initial segment) is critical in the control of pyramidal cell action potential output and synchronization. It has been proposed that the inhibitory synapses targeting pyramidal cell somata, dendritic shafts, and spines differs with regard to their synaptic strength (e.g. Miles et al. 1996; Xue et al. 2014; Kubota et al. 2015). In addition, there is a variability in the density and number of perisomatic GABAergic boutons across layers and cortical areas in the human brain (e.g. Inda et al. 2007; Blázquez-Llorca et al. 2010; Ostos et al. 2023). Thus, an integrative multiscale study at micro-, meso-, and macroscopic levels would be necessary to obtain more comprehensive knowledge about the synaptic organization.

Finally, a number of studies highlighted the interindividual variability in the structural and functional organization of the human brain (Jacobs and Scheibel 1993; Benavides-Piccione et al. 2005; Alonso-Nanclares et al. 2008; Blázquez-Llorca et al. 2010; Benavides-Piccione et al. 2013; Fernández-González et al. 2017; Peng et al. 2019; Montero-Crespo et al. 2020; Domínguez-Álvarez et al. 2021a; Cano-Astorga et al. 2021). In the present study, we have observed that interindividual variability may be related to certain cortical regions and to particular synaptic characteristics—with some regions more variable with regard to the synaptic density (e.g. dBA38), and others more variable with regard to the postsynaptic target distribution (e.g. BA21). Thus, similar or different synaptic characteristics can be found among individuals. The differences between the cortical circuit organization found in the present study between different individuals may suggest adaptations of each individual to particular functions.

## Abbreviation list

3D: three-dimensional, AMPA:  $\alpha$ -amino-3-hydroxy-5-methyl-4-isoxazolepropionic acid, AS: asymmetric synapses, ANOVA: One-way analyses of variance, BA: Brodmann area, CA1: Cornu Ammonis 1, CF: counting frame, CSR: Complete Spatial Randomness, d: dorsal, FIB/SEM: focused ion beam/scanning electron microscopy, KS: Kolmogorov–Smirnov, KW: Kruskal–Wallis, MW: Mann–Whitney, NMDA: N-methyl-D-aspartate, PB: phosphate buffer, PSD: postsynaptic density, SAS: synaptic apposition surface, SE: standard error of the mean, SD: standard deviation, SS: symmetric synapses, v: ventral, Vv: volume fraction,  $\chi^2$ : chi-square.

## Acknowledgments

We would like to thank Carmen Álvarez and Lorena Valdés for their technical assistance, and Nick Guthrie for his excellent editorial assistance.

## CRediT author statement

Nicolás Cano-Astorga (Formal analysis, Investigation, Methodology, Writing—original draft), Sergio Plaza-Alonso (Formal analysis, Methodology, Validation, Writing—review and editing), Javier Defelipe (Conceptualization, Funding acquisition, Supervision, Writing—review and editing), Lidia Alonso-Nanclares (Conceptualization, Data curation, Formal analysis, Supervision, Validation, Writing—review and editing).



## Supplementary material

Supplementary material is available at *Cerebral Cortex* online.

## Funding

This work was supported by the following Grants: PGC2018–094307-B-I00 and PID2021–127924NB-I00 (to J.D.) funded by MCIN/AEI/10.13039/501100011033, CSIC Interdisciplinary Thematic Platform—Cajal Blue Brain (PTI-BLUEBRAIN; Spain) and the European Union's Horizon 2020 Framework Programme for Research and Innovation under Specific Grant Agreement No. 945539 (Human Brain Project SGA3). Research Fellowships funded by MCIN/AEI/10.13039/501100011033 for N.C.-A. (PRE2019-089228) and S.P.-A. (FPU19/00007).

**Conflict of interests statement:** The authors declare that they have no conflict of interest.

## Data Availability

Most data are available in the main text and the [Supplementary Data](#). The datasets used and analyzed during the current study are published in the EBRAINS Knowledge Graph (DOI: [10.25493/B3V0-4D8](#)): Alonso-Nanclares L., Cano-Astorga N., Plaza-Alonso S., DeFelipe J. (2022). “3D ultrastructural study of synapses using FIB/SEM in the Human Cortex (Brodmann areas 24 and 38)”. Human Brain Project Neuroinformatics Platform.

## Ethics approval

Brain tissue samples were obtained following the guidelines and approval of the Institutional Ethical Committee at the School of Medicine, University of Castilla-La Mancha (Albacete, Spain).

## References

- Alonso-Nanclares L, Gonzalez-Soriano J, Rodriguez JR, DeFelipe J. Gender differences in human cortical synaptic density. *PNAS*. 2008;105(38):14615–14619.
- Alonso-Nanclares L, Rodríguez JR, Merchán-Pérez A, González-Soriano J, Plaza-Alonso S, Cano-Astorga N, Naumann RK, Brecht M, DeFelipe J. Cortical synapses of the world's smallest mammal: an FIB/SEM study in the Etruscan Shrew. *J Comp Neurol*. 2023;531(3):390–414.
- Antón-Sánchez L, Bielza C, Merchán-Pérez A, Rodríguez J-R, DeFelipe J, Larrañaga P. Three-dimensional distribution of cortical synapses: a replicated point pattern-based analysis. *Front Neuroanat*. 2014;8:85.
- Baddeley A, Rubak E, Turner R. *Spatial point patterns: methodology and applications* with R. Boca Raton, CA: Chapman and Hall/CRC Press; 2015.
- Barbas H. General cortical and special prefrontal connections: principles from structure to function. *Annu Rev Neurosci*. 2015;38(1):269–289.
- Bartolomeo P, Seidel MT. Hemispheric lateralization of attention processes in the human brain. *Curr Opin Psychol*. 2019;29:90–96.
- Beaulieu C, Kisvarday Z, Somogyi P, Cynader M, Cowey A. Quantitative distribution of GABA-immunopositive and-immunonegative neurons and synapses in the monkey striate cortex (area 17). *Cereb Cortex*. 1992;2(4):295–309.
- Benavides-Piccione R, DeFelipe J. Distribution of neurons expressing tyrosine hydroxylase in the human cerebral cortex. *J Anat*. 2007;211(2):212–222.
- Benavides-Piccione R, Arellano J, DeFelipe J. Catecholamine innervation of pyramidal neurons in the human temporal cortex. *Cereb Cortex*. 2005;15(10):1584–1591.
- Benavides-Piccione R, Fernaud-Espinosa I, Robles V, Yuste R, DeFelipe J. Age-based comparison of human dendritic spine structure using complete three-dimensional reconstructions. *Cereb Cortex*. 2013;23(8):1798–1810.
- Benavides-Piccione R, Rojo C, Kastanauskaite A, DeFelipe J. Variation in pyramidal cell morphology across the human anterior temporal lobe. *Cereb Cortex*. 2021;31(8):3592–3609.
- Blaizot X, Mansilla F, Insausti AM, Constans JM, Salinas-Alamán A, Pró-Sistiaga P, Mohedano-Moriano A, Insausti R. The human parahippocampal region: I. Temporal pole cytoarchitectonic and MRI correlation. *Cereb Cortex*. 2010;20(9):2198–2212.
- Blázquez-Llorca L, García-Marín V, DeFelipe J. GABAergic complex basket formations in the human neocortex. *J Comp Neurol*. 2010;518(24):4917–4937.
- Blázquez-Llorca L, Merchán-Pérez A, Rodríguez JR, Gascon J, DeFelipe J. FIB/SEM technology and Alzheimer's disease: Three-dimensional analysis of human cortical synapses. *J Alzheimer's Dis*. 2013;34(4):995–1013.
- Calì C, Wawrzyniak M, Becker C, Maco B, Cantoni M, Jorstad A, Nigro B, Grillo F, De Paola V, Fua P, et al. The effects of aging on neuropil structure in mouse somatosensory cortex—a 3D electron microscopy analysis of layer 1. *PLoS One*. 2018;13(7):e0198131.
- Cano-Astorga N, DeFelipe J, Alonso-Nanclares L. Three-dimensional synaptic Organization of Layer III of the human temporal neocortex. *Cereb Cortex*. 2021;31(10):4742–4764.
- Chen S, Yu C, Rong L, Li CH, Qin X, Ryu H, Park H. Altered synaptic vesicle release and Ca<sup>2+</sup> influx at single presynaptic terminals of cortical neurons in a knock-in mouse model of Huntington's disease. *Front Mol Neurosci*. 2018;11:478.
- Chindemi G, Abdellah M, Amsalem O, Benavides-Piccione R, Delatre V, Doron M, Ecker A, Jaquier AT, King J, Kumbhar P, et al. A calcium-based plasticity model for predicting long-term potentiation and depression in the neocortex. *Nat Commun*. 2022;13(1):3038.
- Chini M, Pfeffer T, Hanganu-Opatz I. An increase of inhibition drives the developmental decorrelation of neural activity. *Elife*. 2022;11:e78811.
- Chiu CQ, Lur G, Morse TM, Carnevale NT, Ellis-Davies GC, Higley MJ. Compartmentalization of GABAergic inhibition by dendritic spines. *Science*. 2013;340(6133):759–762.
- D'Souza RD, Burkhalter A. A laminar organization for selective cortico-cortical communication. *Front Neuroanat*. 2017;11:71.
- Damasio AR, Tranel D, Damasio H. Face agnosia and the neural substrates of memory. *Annu Rev Neurosci*. 1990;13(1):89–109.
- Damasio H, Grabowski TJ, Tranel D, Hichwa RD, Damasio AR. A neural basis for lexical retrieval. *Nature*. 1996;380(6574):499–505. Erratum in: *Nature*, 1996;381(6595):810.
- DeFelipe J. Types of neurons, synaptic connections and chemical characteristics of cells immunoreactive for calbindin-D28K, parvalbumin and calretinin in the neocortex. *J Chem Neuroanat*. 1997;14(1):1–19.
- DeFelipe J. The evolution of the brain, the human nature of cortical circuits, and intellectual creativity. *Front Neuroanat*. 2011;5:29. Erratum in: *Front Neuroanat*, 2013;7:10.
- DeFelipe J. The anatomical problem posed by brain complexity and size: a potential solution. *Front Neuroanat*. 2015;9:104.
- DeFelipe J, Fairén A. A simple and reliable method for correlative light and electron microscopic studies. *J Histochem Cytochem*. 1993;41(5):769–772.

- DeFelipe J, Fariñas I. The pyramidal neuron of the cerebral cortex: morphological and chemical characteristics of the synaptic inputs. *Prog Neurobiol*. 1992;39(6):563–607.
- DeFelipe J, Hendry SH, Jones EG. Synapses of double bouquet cells in monkey cerebral cortex visualized by calbindin immunoreactivity. *Brain Res*. 1989;503(1):49–54.
- DeFelipe J, Hendry SH, Hashikawa T, Molinari M, Jones EG. A microcolumnar structure of monkey cerebral cortex revealed by immunocytochemical studies of double bouquet cell axons. *Neuroscience*. 1990;37(3):655–673.
- DeFelipe J, Marco P, Busturia I, Merchán-Pérez A. Estimation of the number of synapses in the cerebral cortex: methodological considerations. *Cereb Cortex*. 1999;9(7):722–732.
- DeFelipe J, Alonso-Nanclares L, Arellano J. Microstructure of the neocortex: comparative aspects. *J Neurocytol*. 2002;31(3/5):299–316.
- Dezachy O, Kozak S, Bar-Haim Y, Censor N, Dayan E. Intrinsic functional connectivity of the anterior cingulate cortex is associated with tolerance to distress. *eNeuro*. 2021;8(5):ENEURO.0277-21.2021.
- Ding SL, Van Hoesen GW, Cassell MD, Poremba A. Parcellation of human temporal polar cortex: a combined analysis of multiple cytoarchitectonic, chemoarchitectonic, and pathological markers. *J Comp Neurol*. 2009;514(6):595–623.
- Domínguez-Álvaro M, Montero-Crespo M, Blazquez-Llorca L, Insausti R, DeFelipe J, Alonso-Nanclares L. Three-dimensional analysis of synapses in the transentorhinal cortex of Alzheimer's disease patients. *Acta Neuropathol Commun*. 2018;6(1):20.
- Domínguez-Álvaro M, Montero-Crespo M, Blazquez-Llorca DFJ, Alonso-Nanclares L. 3D electron microscopy study of synaptic organization of the normal human transentorhinal cortex and its possible alterations in Alzheimer's disease. *Eneuro*. 2019;6(4):ENEURO.0140-19.2019.
- Domínguez-Álvaro M, Montero-Crespo M, Blazquez-Llorca L, DeFelipe J, Alonso-Nanclares L. 3D ultrastructural study of synapses in the human entorhinal cortex. *Cereb Cortex*. 2021a;31(1):410–425.
- Domínguez-Álvaro M, Montero-Crespo M, Blazquez-Llorca L, Plaza-Alonso S, Cano-Astorga N, DeFelipe J, Alonso-Nanclares L. 3D analysis of the synaptic organization in the entorhinal cortex in Alzheimer's disease. *eNeuro*. 2021b;8(3):ENEURO.0504-20.2021.
- Eyal G, Verhoog MB, Testa-Silva G, Deitcher Y, Benavides-Piccione R, DeFelipe J, de Kock CPJ, Mansvelder HD, Segev I. Human cortical pyramidal neurons: from spines to spikes via models. *Front Cell Neurosci*. 2018;12:181.
- Felleman DJ, Van Essen DC. Distributed hierarchical processing in the primate cerebral cortex. *Cereb Cortex*. 1991;1(1):1–47.
- Fernández-González P, Benavides-Piccione R, Leguey I, Bielza C, Larrañaga P, DeFelipe J. Dendritic-branching angles of pyramidal neurons of the human cerebral cortex. *Brain Struct Funct*. 2017;222(4):1847–1859.
- Finnema SJ, Nabulsi NB, Eid T, Detyniecki K, Lin SF, Chen MK, Dhaher R, Matuskey D, Baum E, Holden D, et al. Imaging synaptic density in the living human brain. *Sci Transl Med*. 2016;8(348):348ra96.
- Freund TF, Buzsáki G. Interneurons of the hippocampus. *Hippocampus*. 1996;6(4):347–470.
- Fuster JM. Cognitive networks (cognits) process and maintain working memory. *Front Neural Circuits*. 2022;15:790691.
- Ganeshina O, Berry RW, Petralia RS, Nicholson DA, Geinisman Y. Differences in the expression of AMPA and NMDA receptors between axospinous perforated and nonperforated synapses are related to the configuration and size of postsynaptic densities. *J Comp Neurol*. 2004a;468(1):86–95.
- Ganeshina O, Berry RW, Petralia RS, Nicholson DA, Geinisman Y. Synapses with a segmented, completely partitioned postsynaptic density express more AMPA receptors than other axospinous synaptic junctions. *Neuroscience*. 2004b;125(3):615–623.
- Geinisman Y, Morrell F, de Toledo-Morrell L. Axospinous synapses with segmented postsynaptic densities: morphologically distinct synaptic subtype contributing to the number of profiles of 'perforated' synapses visualized in random sections. *Brain Res*. 1987;423(1–2):179–188.
- Geinisman Y, Morrell F, de Toledo-Morrell L. Induction of long-term potentiation is associated with an increase in the number of axospinous synapses with segmented postsynaptic densities. *Brain Res*. 1991;566(1–2):77–88.
- Geinisman Y, de Toledo-Morrell L, Morrell F, Persina IS, Rossi M. Structural synaptic plasticity associated with the induction of long-term potentiation is preserved in the dentate gyrus of aged rats. *Hippocampus*. 1992a;2(4):445–456.
- Geinisman Y, Morrell F, de Toledo-Morrell L. Increase in the number of axospinous synapses with segmented postsynaptic densities following hippocampal kindling. *Brain Res*. 1992b;569(2):341–347.
- Geinisman Y, de Toledo-Morrell L, Morrell F, Heller RE, Rossi M, Parshall RF. Structural synaptic correlate of long-term potentiation: formation of axospinous synapses with multiple, completely partitioned transmission zones. *Hippocampus*. 1993;3(4):435–445.
- Gidon A, Zolnik TA, Fidzinski P, Bolduan F, Papoutsi A, Poirazi P, Holtkamp M, Vida I, Larkum ME. Dendritic action potentials and computation in human layer 2/3 cortical neurons. *Science*. 2020;367(6473):83–87.
- Gray EG. Axo-somatic and axo-dendritic synapses of the cerebral cortex: an electron microscope study. *J Anat*. 1959;4:420–433.
- Gundersen HJG, Bendtsen TF, Korbo L, Marcussen N, Møller A, Nielsen K, Nyengaard JR, Pakkenberg B, Sørensen FB, Vesterby A, et al. Some new, simple and efficient stereological methods and their use in pathological research and diagnosis. *APMIS*. 1988;96(1–6):379–394.
- Hsu A, Luebke JI, Medalla M. Comparative ultrastructural features of excitatory synapses in the visual and frontal cortices of the adult mouse and monkey. *J Comp Neurol*. 2017;525(9):2175–2191.
- Hu H, Vervaeke K. Synaptic integration in cortical inhibitory neuron dendrites. *Neuroscience*. 2018;368:115–131.
- Inda MC, DeFelipe J, Munoz A. The distribution of chandelier cell axon terminals that express the GABA plasma membrane transporter GAT-1 in the human neocortex. *Cereb Cortex*. 2007;17(9):2060–2071.
- Insausti R. Comparative neuroanatomical parcellation of the human and nonhuman primate temporal pole. *J Comp Neurol*. 2013;521(18):4163–4176.
- Jackson RL, Hoffman P, Pobric G, Lambon Ralph MA. The semantic network at work and rest: differential connectivity of anterior temporal lobe subregions. *J Neurosci*. 2016;36(5):1490–1501.
- Jacobs B, Scheibel AB. A quantitative dendritic analysis of Wernicke's area in humans. I. Lifespan changes. *J Comp Neurol*. 1993;327(1):83–96.
- Jones DG, Itarat W, Calverley RKS. Perforated synapses and plasticity: a developmental overview. *Mol Neurobiol*. 1991;5(2–4):217–228.
- Joyce MKP, Marshall LG, Banik SL, Wang J, Xiao D, Bunce JG, Barbas H. Pathways for memory, cognition and emotional context: hippocampal, subgenual area 25, and amygdalar axons show unique interactions in the primate thalamic reuniens nucleus. *J Neurosci*. 2022;42(6):1068–1089.
- Keogh C, Deli A, Zand APD, Zorman MJ, Boccard-Binet SG, Parrott M, Sigalas C, Weiss AR, Stein JF, FitzGerald JJ, et al. Spatial and temporal distribution of information processing in the human dorsal anterior cingulate cortex. *Front in Human Neurosci*. 2022;16:780047.



- Kleinjan MS, Buchta WC, Ogelman R, Hwang IW, Kuwajima M, Hubbard DD, Kareemo DJ, Prikhodko O, Olah SL, Gomez Wulschner LE, et al. Dually innervated dendritic spines develop in the absence of excitatory activity and resist plasticity through tonic inhibitory crosstalk. *Neuron*. 2023;111(3):362–371.e6.
- Kondo H, Saleem KS, Price JL. Differential connections of the temporal pole with the orbital and medial prefrontal networks in macaque monkeys. *J Comp Neurol*. 2003;465(4):499–523.
- Kubota Y, Kondo S, Nomura M, Hatada S, Yamaguchi N, Mohamed AA, Karube F, Lübke J, Kawaguchi Y. Functional effects of distinct innervation styles of pyramidal cells by fast spiking cortical interneurons. *Elife*. 2015;4:e07919.
- Levakov G, Sporns O, Avidan G. Modular community structure of the face network supports face recognition. *Cereb Cortex*. 2021;32(18):3945–3958.
- de Lima AD, Morrison JH. Ultrastructural analysis of somatostatin-immunoreactive neurons and synapses in the temporal and occipital cortex of the macaque monkey. *J Comp Neurol*. 1989;283(2):212–227.
- del Río MR, DeFelipe J. A light and electron microscopic study of Calbindin D-28k immunoreactive double bouquet cells in the human temporal cortex. *Brain Res*. 1995;690(1):133–140.
- Lukacs IP, Francavilla R, Field M, Hunter E, Howarth M, Horie S, Plaha P, Stacey R, Livermore L, Ansorge O, et al. Differential effects of group III metabotropic glutamate receptors on spontaneous inhibitory synaptic currents in spine-innervating double bouquet and parvalbumin-expressing dendrite-targeting GABAergic interneurons in human neocortex. *Cereb Cortex*. 2022;33(5):2101–2142.
- Lüscher C, Malenka RC. NMDA receptor-dependent long-term potentiation and long-term depression (LTP/LTD). *Cold Spring Harb Perspect Biol*. 2012;4(6):a005710.
- Lüscher C, Nicoll RA, Malenka RC, Muller D. Synaptic plasticity and dynamic modulation of the postsynaptic membrane. *Nat Neurosci*. 2000;3(6):545–550.
- Magee JC, Grienberger C. Synaptic plasticity forms and functions. *Ann Rev Neurosci*. 2020;43(1):95–117.
- Mansvelder HD, Verhoog MB, Goriounova NA. Synaptic plasticity in human cortical circuits: cellular mechanisms of learning and memory in the human brain? *Curr Opin Neurobiol*. 2019;54:186–193.
- Markram H, Muller E, Ramaswamy S, Reimann MW, Abdellah M, Sanchez CA, Ailamaki A, Alonso-Nanclares L, Antille N, Arsever S, et al. Reconstruction and simulation of neocortical microcircuitry. *Cell*. 2015;163(2):456–492.
- Matz J, Gilyan A, Kolar A, McCarvill T, Krueger SR. Rapid structural alterations of the active zone lead to sustained changes in neurotransmitter release. *PNAS*. 2010;107(19):8836–8841.
- Merchán-Pérez A, Rodríguez J-R, Alonso-Nanclares L, Schertel A, DeFelipe J. Counting synapses using FIB/SEM microscopy: a true revolution for ultrastructural volume reconstruction. *Front Neuroanat*. 2009;3:18.
- Merchán-Pérez A, Rodríguez J-R, González S, Robles V, DeFelipe J, Larrañaga P, Bielza C. Three-dimensional spatial distribution of synapses in the neocortex: a dual-beam electron microscopy study. *Cereb Cortex*. 2014;24(6):1579–1588.
- Mesulam MM. Temporopolar regions of the human brain. *Brain*. 2022;146(1):awac339–awac341.
- Miles R, Tóth K, Gulyás AI, Hájos N, Freund TF. Differences between somatic and dendritic inhibition in the hippocampus. *Neuron*. 1996;16(4):815–823.
- Montero-Crespo M, Domínguez-Álvaro M, Rondón-Carrillo P, Alonso-Nanclares L, DeFelipe J, Blazquez-Llorca L. Three-dimensional synaptic organization of the human hippocampal CA1 field. *Elife*. 2020;9:e57013.
- Montero-Crespo M, Domínguez-Álvaro M, Alonso-Nanclares L, DeFelipe J, Blazquez-Llorca L. Three-dimensional analysis of synaptic organization in the hippocampal CA1 field in Alzheimer's disease. *Brain*. 2021;144(2):553–573.
- Morales J, Alonso-Nanclares L, Rodríguez JR, Defelipe J, Rodríguez A, Merchán-Pérez A. Espina: a tool for the automated segmentation and counting of synapses in large stacks of electron microscopy images. *Front Neuroanat*. 2011;5:18.
- Morales J, Rodríguez A, Rodríguez J-R, DeFelipe J, Merchán-Pérez A. Characterization and extraction of the synaptic apposition surface for synaptic geometry analysis. *Front Neuroanat*. 2013;7:20.
- Morán MA, Mufson EJ, Mesulam MM. Neural inputs into the temporopolar cortex of the rhesus monkey. *J Comp Neurol*. 1987;256(1):88–103.
- Morecraft RJ, Geula C, Mesulam MM. Architecture of connectivity within a cingulo-fronto-parietal neurocognitive network for directed attention. *Arch Neurol*. 1993;50(3):279–284.
- Nakamura K, Kubota K. The primate temporal pole: its putative role in object recognition and memory. *Behav Brain Res*. 1996;77(1–2):53–77.
- Neuman KM, Molina-Campos E, Musial TF, Price AL, Oh K-J, Wolke ML, Buss EW, Scheff SW, Mufson EJ, Nicholson DA. Evidence for Alzheimer's disease-linked synapse loss and compensation in mouse and human hippocampal CA1 pyramidal neurons. *Brain Struct Funct*. 2016;220(6):3143–3165.
- Olson IR, McCoy D, Klobusicky E, Ross LA. Social cognition and the anterior temporal lobes: a review and theoretical framework. *Soc Cogn Affect Neurosci*. 2013;8(2):123–133.
- Onwordi EC, Halff EF, Whitehurst T, Mansur A, Cotel MC, Wells L, Greeney H, Bonsall D, Rogdaki M, Shatalina E, et al. Synaptic density marker SV2A is reduced in schizophrenia patients and unaffected by antipsychotics in rats. *Nat Commun*. 2020;11(1):246.
- Oorschot D, Peterson D, Jones D. Neurite growth from, and neuronal survival within, cultured explants of the nervous system: a critical review of morphometric and stereological methods, and suggestions for the future. *Prog Neurobiol*. 1991;37(6):525–546.
- Ostos S, Aparicio G, Fernaud-Espinosa I, DeFelipe J, Muñoz A. Quantitative analysis of the GABAergic innervation of the soma and axon initial segment of pyramidal cells in the human and mouse neocortex. *Cereb Cortex*. 2023;33(7):bhac314–bhac3909.
- Palomero-Gallagher N, Zilles K. Cortical layers: cyto-, myelo-, receptor- and synaptic architecture in human cortical areas. *NeuroImage*. 2019;197:716–741.
- Palomero-Gallagher N, Mohlberg H, Zilles K, Vogt B. Cytology and receptor architecture of human anterior cingulate cortex. *J Comp Neurol*. 2008;508(6):906–926.
- Paquola C, Seidlitz J, Benkarim O, Royer J, Klimes P, Bethlehem RAI, Larivière S, Vos de Wael R, Rodríguez-Cruces R, Hall JA, et al. A multi-scale cortical wiring space links cellular architecture and functional dynamics in the human brain. *PLoS Biol*. 2020;18(11):e3000979.
- Pascual B, Masdeu JC, Hollenbeck M, Makris N, Insausti R, Ding SL, Dickerson BC. Large-scale brain networks of the human left temporal pole: a functional connectivity MRI study. *Cereb Cortex*. 2015;25(3):680–702.
- Peng Y, Mittermaier FX, Planert H, Schneider UC, Alle H, Geiger JRP. High-throughput microcircuit analysis of individual human

- brains through next-generation multineuron patch-clamp. *Elife*. 2019;8:e48178.
- Peters A, Palay SL, Webster HD. *The fine structure of the nervous system: the neurons and their supporting cells*. New York, NY: Oxford University; 1991.
- Peters A, Sethares C, Luebke JI. Synapses are lost during aging in the primate prefrontal cortex. *Neuroscience*. 2008;152(4):970–981.
- Radhakrishnan A, Li X, Grushin K, Krishnakumar SS, Liu J, Rothman JE. Symmetrical arrangement of proteins under release-ready vesicles in presynaptic terminals. *PNAS*. 2021;118(5):e2024029118.
- Rizzoli SO, Betz WJ. Synaptic vesicle pools. *Nat Rev Neurosci*. 2005;6(1):57–69.
- Rockland KS. What do we know about laminar connectivity? *NeuroImage*. 2019;197:772–784.
- Rollenhagen A, Walkenfort B, Yakoubi R, Klauke SA, Schmuhl-Giesen SF, Heinen-Weiler J, Voortmann S, Marshallsay B, Palaz T, Holz U, et al. Synaptic organization of the human temporal lobe neocortex as revealed by high-resolution transmission, focused ion beam scanning, and electron microscopic tomography. *Int J Mol Sci*. 2020;21(15):5558.
- Santuy A, Rodríguez J-R, DeFelipe J, Merchán-Pérez A. Study of the size and shape of synapses in the juvenile rat somatosensory cortex with 3D electron microscopy. *eNeuro*. 2018a;5(1):ENEURO.0377–17.2017.
- Santuy A, Rodríguez J-R, DeFelipe J, Merchán-Pérez A. Volume electron microscopy of the distribution of synapses in the neuropil of the juvenile rat somatosensory cortex. *Brain Struct Funct*. 2018b;223(1):77–90.
- Santuy A, Tomás-Roca L, Rodríguez JR, González-Soriano J, Zhu F, Qiu Z, Grant SGN, DeFelipe J, Merchán-Pérez A. Estimation of the number of synapses in the hippocampus and brain-wide by volume electron microscopy and genetic labeling. *Sci Rep*. 2020;10(1):14014. <https://doi.org/10.1038/s41598-020-70859-5>.
- Schmuhl-Giesen S, Rollenhagen A, Walkenfort B, Yakoubi R, Sätzler K, Miller D, von Lehe M, Hasenberg M, Lübke JHR. Sublamina-specific dynamics and ultrastructural heterogeneity of layer 6 excitatory synaptic boutons in the adult human temporal lobe neocortex. *Cereb Cortex*. 2022;32(9):1840–1865.
- Schubert D, Kötter R, Staiger JF. Mapping functional connectivity in barrel-related columns reveals layer- and cell type-specific microcircuits. *Brain Struct Funct*. 2007;212(2):107–119.
- Sohal VS, Rubenstein JLR. Excitation-inhibition balance as a framework for investigating mechanisms in neuropsychiatric disorders. *Mol Psychiatry*. 2019;24(9):1248–1257.
- Somogyi P, Cowey A. Combined Golgi and electron microscopic study on the synapses formed by double bouquet cells in the visual cortex of the cat and monkey. *J Comp Neurol*. 1981;195(4):547–566.
- Somogyi P, Tamás G, Lujan R, Buhl EH. Salient features of synaptic organisation in the cerebral cortex. *Brain Res Rev*. 1998;26(2–3):113–135.
- Sporns O, Zwi JD. The small world of the cerebral cortex. *Neuroinformatics*. 2004;2(2):145–162.
- Sporns O, Tononi G, Kötter R. The human connectome: a structural description of the human brain. *PLoS Comput Biol*. 2005;1(4):e42.
- Spruston N. Pyramidal neurons: dendritic structure and synaptic integration. *Nat Rev Neurosci*. 2008;9(3):206–221.
- Sumi T, Harada K. Mechanism underlying hippocampal long-term potentiation and depression based on competition between endocytosis and exocytosis of AMPA receptors. *Sci Rep*. 2020;10(1):1–14.
- Thomson AM, Lamy C. Functional maps of neocortical local circuitry. *Front Neurosci*. 2007;1(1):19–42.
- Toni N, Buchs PA, Nikonenko I, Povilaitite P, Parisi L, Muller D. Remodeling of synaptic membranes after induction of long-term potentiation. *J Neurosci*. 2001;21(16):6245–6251.
- Tremblay R, Lee S, Rudy B. GABAergic interneurons in the neocortex: from cellular properties to circuits. *Neuron*. 2016;91(2):260–292.
- Turégano-López M, DeFelipe J, Merchán-Pérez A. Ultraestructura y conectividad de la corteza cerebral. Doctoral Thesis. Madrid (Spain): Autonoma University of Madrid; 2022.
- Van Essen DC, Smith SM, Barch DM, Behrens TE, Yacoub E, Ugurbil K, WU-Minn HCP Consortium. The WU-Minn Human Connectome Project: an overview. *NeuroImage*. 2013;80:62–79.
- Villa KL, Berry KP, Subramanian J, Cha JW, Oh WC, Kwon HB, Kubota Y, So PT, Nedivi E. Inhibitory synapses are repeatedly assembled and removed at persistent sites in vivo. *Neuron*. 2016;89(4):756–769.
- Wang J, John Y, Barbas H. Pathways for contextual memory: the primate hippocampal pathway to anterior cingulate cortex. *Cereb Cortex*. 2021;31(3):1807–1826.
- Xu Y, Lin Q, Han Z, He Y, Bi Y. Intrinsic functional network architecture of human semantic processing: Modules and hubs. *NeuroImage*. 2016;132:542–555.
- Xue M, Atallah BV, Scanziani M. Equalizing excitation-inhibition ratios across visual cortical neurons. *Nature*. 2014;511(7511):596–600.
- Yakoubi R, Rollenhagen A, von Lehe M, Shao Y, Sätzler K, Lübke JHR. Quantitative three-dimensional reconstructions of excitatory synaptic boutons in layer 5 of the adult human temporal lobe neocortex: a fine-scale electron microscopic analysis. *Cereb Cortex*. 2019a;29(7):2797–2814.
- Yakoubi R, Rollenhagen A, von Lehe M, Miller D, Walkenfort B, Hasenberg M, Sätzler K, Lübke JH. Ultrastructural heterogeneity of layer 4 excitatory synaptic boutons in the adult human temporal lobe neocortex. *Elife*. 2019b;8:e48373.
- Zachlod D, Bludau S, Cichon S, Palomero-Gallagher N, Amunts K. Combined analysis of cytoarchitectonic, molecular and transcriptomic patterns reveal differences in brain organization across human functional brain systems. *NeuroImage*. 2022;257:119286.
- Zilles K, Amunts K. Centenary of Brodmann's map conception and fate. *Nat Rev Neurosci*. 2010;11(2):139–145.
- Zilles K, Palomero-Gallagher N. Multiple transmitter receptors in regions and layers of the human cerebral cortex. *Front Neuroanat*. 2017;11:78.